Vibrational Pooling and Constrained Equilibration on Surfaces

Thesis by

E. T. D. Boney

In Partial Fulfillment of the Requirements

for the Degree of

Doctor of Philosophy

California Institute of Technology

Pasadena, California

2014

(Defended September, 27, 2013)

For you, thanks for reading.

Acknowledgments

Who knows how long it took Mike Slackenerny? After seven years, I appear to have finally done enough to graduate.

My supporting cast of characters is wide, and I do not thank them enough. First, thanks go to my wife Susanna, whose support has helped me through the long laborious years. I love you, Mrs. Dooley Boney; thank you for all the bike rides to concerts, across the Black Rock Desert, and all the sunsets down at the Japes.

Secondly, I must thank my family for raising me with an appreciation of science and knowledge, and raising me safe and sound as well. Mom and dad, thank you.

Scientifically, I have the most debt to my advisor, Rudy Marcus, and I will spend a few winding paragraphs thanking him. I came to Caltech because Rudy had not changed his research philosophy his whole career: theory guided first and foremost by interesting experiments. If you cannot explain what people are interested in, then what is your theory good for?

His philosophy is unique, and in my work with him, Rudy has never given in to my urge to publish prematurely. We did not explain experimental results that wound up retracted with my first big paper; this prudence was his, not mine. When that retraction wound up wasting about four years of mean-field work on H:Si(111) and other surfaces, his focus on experiments guided us.

In the end, we found some cool fluorescence results from the late 1980s and early 1990s, and explained vibrational population inversion on surfaces in a way that has previously been done in gases by Treanor. Such inversion could change every sort of measurement at surfaces, not just old fluorescence experiments, from STM and AFM to SFG and SHG, there is now a new possibility besides defect, bridge, dimer or trimer that demands consideration: the vibrational pool! Because of his inkling that we had more to discover, we were able to do unifying work between the gas phase and interfaces that I find very philosophically satisfying in a way that has nothing, and everything, to do with experiment.

Other advice of his that cannot be ignored by anyone searching here for his wisdom is to know the literature. Because we want to be guided by experimental results, we have to find and correctly interpret the existing data as soon as we can. If we reach the bounds of the literature and have not gotten the answer we need, we have to move on until experiment gives us something more to work

with. Along those lines, I owe a great debt to Huan-Cheng Chang, Hugh Richardson, George Ewing, Chifuru Noda, Steven Corcelli, Phillippe Guyot-Sionnest, and John Tully, who did the bulk of the experimental and theoretical work underpinning my thesis. Without them, I would not have had anything to do. I owe a special debt to collaborator Jim Lyons, who developed the isotope mixing code and edited the chapter on self-shielding.

Besides advice from Rudy, I also benefited greatly from the comments of my committee, and thank them now by name for their general wisdom as well as cumulative specific advice: Rob Phillips, Aron Kupperman, Tom Miller, and Jim Heath.

Furthermore, in my time at Caltech, I have had the opportunity to know unique individuals that have shaped my way of thinking about the world in positive and permanent ways. They are, in no particular order (lots of Doctors, so forget the honorifics): Nima Ghaderi, Oliver Eslinger, Jorge Cham, Jonny Haug, Allyce Ozarski, Lauren Lebon, Nicolas LaCasse, Sanza Kazadi, Andy Downard, Glenn Garrett, Michael Shearn, Dan Riley, Anna Beck, Faisal Amlani, Paul Minor, Jerry Maine, Alex Romero, Vahe Gabuchian, Drew Kennedy, Meg Rosenberg, Meher Ayalasomayajula, Yousung Jung, Maksym Kryvohuz, Nick Agich, Josh Moorhead, J. P. Chism, Brian Duistermars, Young-In Oh, Ronnie Bryan, Artur Menzeleev, Jason Goodpaster, Rosemary Rohde, Scott Kelber, Geoffrey Lovely, Travis Essl, Chris Daeffler, Ian Tonks, Nathan Hodas, Wei-Chen Chen, Zhaoyan Zhu, Yun-Hua Hong, and Sandor Volkan-Kacso. I also have had several cats whose company I have enjoyed thoroughly, despite my cat allergies: Mrs. Kitty, LadyBird Johnson, Trash Cat, and Flea, you were all good kitties.

At MIT, I developed my love of theoretical physical science combined with video games, automaton programming competitions, ten consecutive Mystery Hunts, Hoegaarden, and philosophical musings, thanks in large parts to MIT dorm mates who remain some of my closest friends: Dennis Wei, Billy Waldman, Sheel Dandekar, Jon Ursprung, Downtown Twarog, Robert Jason Harris, Gabe Durazo, and Michael Mooney. I may stand on the shoulders of great scientists I'll never meet in my research, but I stood with you in reality, contemplating the wonders of the universe from a revolutionary war park in the dead of night.

Finally, it would be remiss of me not to thank the ARO, ONR, and NSF for their financial support of this research.

Abstract

In this thesis, we provide a statistical theory for the vibrational pooling and fluorescence time dependence observed in infrared laser excitation of CO on an NaCl surface. The pooling is seen in experiment and in computer simulations. In the theory, we assume a rapid equilibration of the quanta in the substrate and minimize the free energy subject to the constraint at any time t of a fixed number of vibrational quanta $N(t)$. At low incident intensity, the distribution is limited to one-quantum exchanges with the solid and so the Debye frequency of the solid plays a key role in limiting the range of this one-quantum domain. The resulting inverted vibrational equilibrium population depends only on fundamental parameters of the oscillator (ω_e and $\omega_e\chi_e$) and the surface (ω_D and T). Possible applications and relation to the Treanor gas phase treatment are discussed. Unlike the solid phase system, the gas phase system has no Debye-constraining maximum. We discuss the possible distributions for arbitrary N-conserving diatom-surface pairs, and include application to H:Si(111) as an example.

Computations are presented to describe and analyze the high levels of infrared laser-induced vibrational excitation of a monolayer of absorbed ^{13}CO on a NaCl(100) surface. The calculations confirm that, for situations where the Debye frequency limited n domain restriction approximately holds, the vibrational state population deviates from a Boltzmann population linearly in n. Nonetheless, the full kinetic calculation is necessary to capture the result in detail.

We discuss the one-to-one relationship between N and γ and the examine the state space of the new distribution function for varied γ. We derive the Free Energy, $F = N\gamma kT - kTln(\sum P_n)$, and effective chemical potential, $\mu_n \approx \gamma kT$, for the vibrational pool. We also find the anti correlation of neighbor vibrations leads to an emergent correlation that appears to extend further than nearest neighbor.

Contents

Acknowledgments **iv**

Abstract **vi**

1 Theory of Vibrational Equilibria and Pooling at Solid-Diatom Interfaces **5**

1.1 Introduction 5

1.2 Statistical Treatment Of Vibrational Energy Distribution 6

1.3 Resulting Dynamics 7

1.4 Discussion 9

1.5 Conclusions 13

2 On the Infrared Fluorescence of Monolayer ^{13}CO:NaCl(100) **14**

2.1 Introduction 14

2.2 Vibrational Exchange for monolayer CO 15

2.3 Kinetic Monte Carlo Results 17

2.4 Discussion 18

2.5 Conclusions 20

2.6 Chapter Appendix A: Rate constants 21

2.7 Chapter Appendix B: Units 22

3 Vibrational Pools at Solid-Diatom Interfaces: Chemical Potential and Emergent Correlation **30**

3.1 Introduction 30

3.2 Formation of higher pools 30

3.3 Evaluation of P_n for several N and γ 31

3.4 Analysis of the Correlation Function vs. Distance of Separation 32

3.5 Introduction of the Free Energy and Chemical Potential 34

3.6 Results and Discussion 36

3.7 Conclusions 38

4 On the Laser-Induced Desorption of H_2 from an H:Si(111) surface 39

4.1 Background and Introduction 39

4.2 Results 41

4.3 Discussion 43

4.4 Conclusions 47

5 Self-shielding in the $E^1\Pi(1)$-$X^1\Sigma_g^+(0)$ band of CO in a hot solar nebula 48

5.1 Introduction and Background 48

5.2 Computation of Absorption Spectra 51

5.3 Line-by-line calculation of CO photodissociation 54

5.4 Comparison with Navon and Wasserburg 59

5.5 Absorption by H_2 60

5.6 Conclusions 61

5.7 Chapter Appendix: Voigt Profile Approximation 63

List of Figures

1.1 The fit for the parameter, γ. The representative pool is derived from monolayer populations, calculated elsewhere by kinetic Monte Carlo,[1] as the slope of $ln(P_n) + E_n/kT$, vs. n, the vibrational state. For the P_n calculated near the end of a pulse of the conditions of the previous monolayer experiment,[2] $\gamma = 131$. 8

1.2 This figure shows the P_n from Eq. 1.4 compared to the Boltzmann distribution at 22K for $\gamma = 131$. 8

1.3 Calculated $1/\lambda(t)$ versus time, compared with the single exponential observation. . . 10

1.4 The total overtone fluorescence decay (circles computed) matches experiment (solid single exponential with τ=4.3 ms). 10

2.1 Comparison of relevant rate constants: (a) first-order rate constants of relaxation (κ_n), fluorescence ($k_n^{\Delta v=1}$) and overtone fluorescence($k_n^{\Delta v=2}$) (b) second-order rate constants of pooling ($W_{n,m}^p$ for m =1,10 and 20). The second order effect of pooling to state n from an $m = 1$ state which requires an additional phonon to transfer to $n \geq 10$, and so $W_{10,1}^p \approx 10^{-3} W_{9,1}^p$. As second order rate constants, the pooling and depooling rate constants should be multiplied by a conditional probability if one wishes to compare with the first order rate constants, leading to units [s^{-1} per unit conditional probability $P(m|n)$], as discussed in Chapter Appendix B. 23

2.2 The total overtone fluorescence decay (circles computed) matches experiment (solid single exponential, $I(t) = I(0)exp(-t/\tau)$, with time constant τ=4.3 ms). 24

2.3 The vibrational population 6 μs following beginning of pulse (near end of lasing). . . 24

2.4 The vibrational population 1 ms following the beginning of lasing. 25

2.5 The fit of the computed results to the theory-based expression permits the evaluation of statistical parameter $\gamma = 130$, from the slope of the linear fit on the restricted n domain. A typical result for P_n after 4 ms following monolayer excitation is displayed, although this γ is representative of those where the restricted n-domain assumption holds. 25

2.6 The theoretical dispersed fluorescence (assuming perfect collection efficiency) for a monolayer under the experimental monolayer lasing conditions (k_{abs}=9 x $10^4 s^{-1}$), integrated over a (a) 1 ms and (b) 20 ms period after the beginning of lasing.[2] The temporal integration was calculated trapezoidally from $P_n(t)$ at 79 time points spread equally over the length of calculation. 26

2.7 The theoretical dispersed fluorescence (assuming perfect collection efficiency) after (a) 1 ms and (b) 8 ms following CLIO excitation of a monolayer (averaged over a macro pulse for the highest fluence currently available at that wavelength, $k_{abs,CLIO}$ = 5 x$10^7 s^{-1}$ for 8 μs, or 20 mJ). We note that, in (a), the appearance of a tiny higher n shoulder around n = 22 (which is even more pronounced as a relative peak at shorter times, not shown), but that the signal on the ms timescale is overwhelmed by fluorescence from lower n and the distribution becomes the same as that for the monolayer under continued observation. 27

2.8 Snapshots of the theoretical dispersed fluorescence for a monolayer under the experimental monolayer lasing conditions (k_{abs}=9 x $10^4 s^{-1}$). The snapshots given are (a) 1 μs between 77 and 78 μs following beginning of excitation and (b) 12.7 μs period ending 1 ms after the beginning of lasing, representative of the difference in results at different temporal resolutions of collection. 28

2.9 The vibrational population of the surface for a single trajectory at the conclusion of a CLIO FEL pulse (figure (a), 8 μs excitation) and 1 ms thereafter (figure (b), $k_{abs,CLIO}$ = 5 x$10^7 s^{-1}$ for 8 μs excitation for both). For (a), the legend is: n=0-black, 10-red, 20-orange, 25-yellow, 32-white, highest level. For (b) : n=0-black, 5-red, 10-yellow, 12-white, highest level. 29

3.1 This figure shows the formation of P_2, noting $P_{1,ss} \approx 0.5$ 31

3.2 This figure shows N vs. γ for the domain restricted theory. 32

3.3 This figure shows the P_n compared to the Boltzmann distribution at 22K for $\gamma = 130$. 33

3.4 This figure shows the P_n compared to the Boltzmann distribution at 22K for $\gamma = 125$. 33

3.5 This figure shows the P_n compared to the Boltzmann distribution at 22K for $\gamma = 140$. 34

3.6 The vibrational pairwise population 1 ms following the beginning of lasing, compared with the mean-field expectation of the pair considered, the dashed lines are guides for the eye: (black)- $P_{10,0}$, the pairwise probability of a $n = 10$ state next to a $n = 0$ state (orange)-$P_{10,10}$, the pairwise probability of a $n = 10$ state next to a $n = 10$ state (note complete anti-correlation of nearest neighbors). The mean field result for $P_{10,0}$ and $P_{10,10}$ are given by the horizontal lines. Note that, for neighbors, mean-field is a bad approximation, but for $R >> R_0$, the nearest neighbor distance of 3.96 Angstroms, mean-field is recovered. 35

3.7 In this figure, we see F vs. N, and see the chemical potential (slope) is 2120 cm^{-1}. From γkT in our prior work, we had estimated 1960 cm^{-1} based on γ from the domain restricted theory. 37

3.8 The fit of γNkT for 20 ms following Monolayer lasing.[2;1;3] 37

3.9 The fit of γNkT for 30 ms following CLIO lasing.[3] 38

4.1 The fit to the experimental loss of P_1,[4] $\kappa_1 = 1/(5\text{x}10^{-9})$ s^{-1} 42

4.2 The P_n vs. n 1.9 ns after lasing with prior conditions.[4] 43

4.3 Snapshots of the evolution of H_2 from a 50x50 surface under FEL excitation: (a) after 100 ns (b)after 500 ns (c) after 1μs (d) halfway through lasing. We note that the colors indicate black for $n = 0$ white for $n = 21$ in (b)-(d), with $n = 21$, outside the $n = 1-20$ domain, used to mark the sites that have evolved off the surface by associative desorption (white). While we are unable to render the 111 surface (a hexagonal lattice), the square lattice connectivity in figures shown includes diagonals up and to the right and down and to the left of each site, effectively giving 6 neighbors of equal distance. Thus we see diagonally desorbed molecules on the square lattice representation of the 111 surface. 44

4.4 Yield of H_2 after a single macropulse vs. Power of macropulse, assuming fast-pooling (calculations shown for $\mu' = 1e$). 45

5.1 A visual representation of the Aikawa-Herbst model. The colors indicate the number densities of molecular hydrogen (red-highest, yellow-medium high, green-medium low, blue- lowest). The arrows in the negative z-direction indicate the direction of incident intensity. The spirals at large R are representative of vertical mixing. Their amplitude indicates the strength of the mixing. Reproduced with permission.[5] 50

5.2 A comparison of the Voigt, Lorentzian, and Gaussian lineshape for a single transition. 52

5.3 (a) The synthetic $^{12}C^{16}O$ spectrum calculated at 300K. (b) Reproduced from Stark et. al.[6] 55

5.4 The synthetic $^{12}C^{16}O$ spectrum calculated at 50K (black), 300K (red), and 1500K (blue). The 50K and 1500K spectra have been shifted -/+0.5 nm respectively for clarity. The ratio of maxima is approximately 12:4:1. 56

5.5 The spectra for the $X^1\Sigma_g^+(0)$ - $E^1\Pi(1)$ transition of $^{12}C^{16}O$, $^{12}C^{17}O$, and $^{12}C^{18}O$ at 1500 K 56

5.6 The bandhead in the $^{12}C^{18}O$ spectrum at 1500 K 57

5.7 Evidence of a bandhead. This graph shows a bandhead between the 66th and 67th rotational state for $^{12}C^{18}O$. 57

5.8 3-isotope plot at 30 AU with temperature dependent CO cross sections. H_2 absorption by shielding function.[7] 60

5.9 The three isotopomers of $^{12}C^xO$ with a fictitiously high natural linewidth are compared. 61

5.10 (a) $^{12}C^{17}O$, (b) $^{12}C^{16}O$, and (c) $^{12}C^{18}O$ cross section (red) with overlay of H_2 transmission (black). Q-branch of $C^{17}O$ coincides with H_2 transmission feature causing the vertical 3-isotope trajectory at high temperatures. 62

5.11 3-isotope plot with H_2 absorption cross sections at 0.035 AU, 0.87 AU, and 30 AU at the mid-plane (Z=0). 63

List of Tables

2.1 The calculation times and results for a single trajectory on a 100x100 grid with three different resonant rate conditions 1ms following monolayer excitation. They each have relative peaks at $n = 10$, not shown. 18

5.1 Molecular Constants for the various isotopomers of CO in the X^1S_g ground state. All values given in cm^{-1}. Note that e-parity is used for the P and R branches and f-parity is used for the Q branch. 51

5.2 Molecular Constants for the various isotopomers of CO in the E^1P excited state. All values given in cm^{-1}. Note that e-parity is used for the P and R branches and f-parity is used for the Q branch. 51

5.3 Comparison of $f_{v'',v'}$ for different isotopomers. All values from Eidelsberg.[8] 53

Bibliography

[1] E. T. D. Boney and R. A. Marcus, J Chem Phys, **139**, 124107 (2013).

[2] H.-C. Chang and G. E. Ewing, Phys. Rev. Lett., **65**, 2125 (1990).

[3] E. T. D. Boney and R. A. Marcus, J Chem Phys (accepted, A13.08.0077).

[4] P. Guyot-Sionnest, P. Dumas, and Y. J. Chabal, J. Electron Spectrosc. Relat. Phenom., **54/55**, 27 (1990).

[5] Lyons, J. R., personal communication.

[6] G. Stark, P. L. Smith, K. Ito, and K. Yoshino, Astrophys. J., **395**, 705 (1992).

[7] S. R. McCandliss, Pub. Astron. Soc. Pac., **115**, 651 (2003).

[8] M. Eidelsberg, J. J. Benayoun, Y. Viala, and F. Rostas, Astron. and Astrophy. Supplement Series, **90**, 231 (1991).

[9] S. A. Corcelli and J. C. Tully, J Phys Chem A, **106**, 10849 (2002).

[10] S. A. Corcelli and J. C. Tully, J. Chem. Phys., **116** (2002).

[11] H.-C. Chang and G. E. Ewing, J Chem. Phys., **94**, 7635 (1990).

[12] H.-C. Chang and G. E. Ewing, J Chem. Phys., **92**, 7635 (1990).

[13] C. E. Treanor, J. W. Rich, and R. G. Rehm, J. Chem. Phys., **48**, 1798 (1968).

[14] D. McQuarrie, *Statistical Mechanics* (University Science Books, 2000).

[15] C. Kittel, *Introduction to Solid State Physics (8^{th} ed.)* (John Wiley & Sons, 2004).

[16] P. Guyot-Sionnest, Phys. Rev. Lett., **67** (1991).

[17] I. H. Bachir, R. Charneau, and H. Dubost, Chem. Phys., **177**, 675 (1993).

[18] H. Gai and G. A. Voth, J. Chem. Phys., **99** (1993).

[19] J. Ma, E. Wang, Z. Zhang, and B. Wu, Phys. Rev. B, **78** (2008).

[20] Z. Liu, L. C. Feldman, N. H. Tolk, Z. Zhang, and P. I. Cohen, Science, **312**, 1024 (2006).

[21] H.-C. Chang, C. Noda, and G. E. Ewing, J. Vac. Sci. Tech., **8**, 2644 (1990).

[22] H.-C. Chang, H. H. Richardson, and G. E. Ewing, J Chem. Phys., **89**, 7561 (1988).

[23] H.-C. Chang and G. E. Ewing, Chem. Phys., **139**, 55 (1989).

[24] K. A. Fichthorn and W. H. Weinberg, J. Chem. Phys., **95**, 1090 (1991).

[25] L. Aleese, A. Simon, T. McMahon, J.-M. Ortega, D. Scuderi, J. Lemaire, and P. Maitre, International Journal of Mass Spectrometry, **249-250**, 14 (2006).

[26] D. S. Anex and G. E. Ewing, J. Phys. Chem., **90**, 1604 (1986).

[27] H.-C.Chang, personal communication.

[28] P. F. Bernath, *Spectra of Atoms and Molecules* (Oxford University Press, 2005).

[29] J. A. C. Gallas, Phys. Rev. A., **21**, 1829 (1980).

[30] G. S. Higashi, Y. J. Chabal, G. W. Trucks, and K. Raghavachari, Appl. Phys. Lett., **56** (1989).

[31] Y. Chabal, P. Dumas, and P. Guyot-Sionnest, Phys. Rev. Lett., **64** (1990).

[32] P. Jakob and Y. Chabal, J Chem Phys, **95** (1991).

[33] P. Jakob, Y. J. Chabal, and K. Raghavachari, Chem. Phys. Lett., **187** (1991).

[34] M. A. Hines, Y. J. Chabal, T. D. Harris, and A. L. Harris, J Chem Phys, **101** (1994).

[35] P. Guyot-Sionnest, P. H. Lin, and E. M. Miller, J. Chem. Phys., **102** (1995).

[36] R. Honke, P. Jakob, Y. J. Chabal, A. Dvorak, S. Tausendpfund, W. Stigler, P. Pavone, A. P. Mayer, and U. Shroder, Phys. Rev. B, **59** (1999).

[37] P. Dumas and e. al., Phys. Rev. Lett., **65** (1990).

[38] H. Sano and S. Ushioda, Phys. Rev. B, **53** (1996).

[39] P. Gupta, V. L. Colvin, and S. M. George, Phys. Rev. B, **37** (1988).

[40] G. A. Reider, U. Hofer, and T. F. Heinz, J. Chem. Phys., **94** (1990).

[41] H. H. Richardson, G.-C. Chang, C. Noda, and G. E. Ewing, Surf. Sci., **216**, 93 (1989).

[42] B. G. Koehler, C. H. Mak, D. A. Arthur, P. A. Coon, and S. M. George, J Chem. Phys., **89** (1988).

[43] B. Wu, P. I. Cohen, L. C. Feldman, and Z. Zhang, Appl. Phys. Lett., **84** (2004).

[44] Y. Miyauchi, H. Sano, J. Okada, H. Yamashita, and G. Mizutani, Surf. Sci., **603**, 2972 (2009).

[45] Y. Amelin, A. N. Krot, I. D. Hutcheon, and A. A. Ulyanov, Science, **297**, 1678 (2002).

[46] R. N. Clayton, L. Grossman, and T. K. Mayeda, Science, **182**, 485 (1973).

[47] R. N. Clayton, L. Grossman, and T. K. Mayeda, Nature, **415**, 860 (2002).

[48] J. R. Lyons and E. D. Young, Lunar Planet. Sci. Conf. XXXIV, abst. 1981 (2003).

[49] Q.-Z. Yin, Science, **305**, 1729 (2004).

[50] E. F. van Dishoeck and J. F. Black, Astrophys. J., **334**, 771 (1988).

[51] K. I. Öberg, H. Linnartz, R. Visser, and E. F. van Dishoeck, Astrophys. J., **693**, 1209 (2009).

[52] J. R. Lyons and E. D. Young, Nature, **435**, 317 (2005).

[53] R. A. Marcus, J. Chem. Phys., **121**, 8201 (2004).

[54] K. D. McKeegan, A. P. A. Kallio, V. S. Heber, G. Jarzebinski, P. H. Mao, C. D. Coath, T. Kunihiro, R. C. Wiens, J. E. Nordholt, R. W. Moses, D. B. Reisenfeld, A. J. G. Jurewicz, and D. S. Burnett, Science, **332**, 1528 (2011).

[55] H. E. Heidenreich and M. H. Thiemens, Science, **219**, 1073 (1983).

[56] K. Mauerseberger, Geophys. Res. Lett., **8**, 935 (1981).

[57] M. M. Abbas, J. Guo, B. Carli, F. Mencaraglia, M. Carlotti, and I. G. Nolt, J. Geophys. Res., **92**, 13231 (1987).

[58] B. Carli and J. H. Park, J. Geophys. Res., **93**, 3851 (1988).

[59] E. J. Moyer, F. W. Irion, Y. L. Yung, and M. R. Gunson, Geophys. Res. Lett., **23**, 2377 (1996).

[60] D. Krankowsky, P. Lämmerzahl, and K. Mauersberger, Geophys. Res. Lett., **23**, 2377 (1996).

[61] O. Navon and G. J. Wasserburg, Earth Planet. Sci. Lett., **73**, 1 (1985).

[62] Y. Q. Gao and R. A. Marcus, Science, **293**, 259 (2001).

[63] Y. Aikawa and E. Herbst, Astron. Astrophys., **371**, 1107 (2001).

[64] W. Ubacs, I. Velchev, and P. Cacciani, J. Chem. Phys., **113**, 547 (2000).

[65] K.-N. Liou, *Radiation and Cloud Processes in the Atmosphere: Theory, Observation, and Modeling* (Oxford University Press, 2001).

[66] P. F. Bernath, *Handbook of Molecular Physics and Quantum Chemistry: Volume 3: Molecules in the Physicochemical Environment: Spectroscopy, Dynamics and Bulk Properties* (John Wiley and Sons, Ltd., 2002).

[67] H.-H. Lee, E. Herbst, G. Pineau des Forêts, E. Roueff, and J. Le Bourlot, Astron. Astrophys., **311**, 690 (1996).

[68] G. Herzberg, *Spectra of Diatomic Molecules* (Litton Education Publishing, Inc., 1950).

[69] J. W. Sutherland, Symp. Int. Combust. Proc., **21**, 929 (1986).

[70] D. L. Baulch, C. J. Cobos, R. A. Cox, C. Esser, P. Frank, J. Th., J. A. Kerr, M. J. Pilling, J. Troe, R. W. Walker, and J. Warnatz, J. Phys. Chem. Ref. Data, **21**, 411 (1992).

[71] S. Jaffe and F. S. Klein, Far. Soc. Trans., **62**, 3135 (1966).

Chapter 1

Theory of Vibrational Equilibria and Pooling at Solid-Diatom Interfaces

1.1 Introduction

Recently, the infrared absorption of CO on NaCl at low temperatures was calculated using Monte Carlo.[9;10] In this chapter, we describe such a statistical theory to explain two key effects:[9;10;1;11;12] (1) an inversion of the population of CO vibrational states and (2) the origin of the single exponential overtone fluorescence decay, the many contributing second-order and first-order steps in the mechanism notwithstanding.

The present statistical form is of the same type as that derived by Treanor[13] for pooling of vibrational energy, except that since his treatment dealt with gases, he did not have a Debye cutoff. A comparison and possible extension of Treanor's results are given in Section 1.4.

A relative inverted peak in the vibrational population distribution is possible when there is a phonon bottleneck, e.g. when the average energy of the phonons emitted by a pooling step to reach a still higher vibrational state n exceeds $\hbar\omega_D$, where ω_D is the Debye frequency of the solid. This situation is somewhat unusual, because it requires there are no low energy electronic, rotational, bending or vibrational transitions with which the high frequency stretch, in this case CO, can decay in less than a large number of quanta, resulting in relaxation on the ms timescale.[2]

In this work, we derive an expression for the approximate statistics and dynamics of single-phonon processes up to the first pooling maximum, recognizing that higher fluence results may lead to other, higher local maxima in n, a result we probe separately.[1]

1.2 Statistical Treatment Of Vibrational Energy Distribution

In the theory, we assume that after injection of infrared quanta, vibrational pooling and depooling lead to rapid equilibration among the vibrational states of the system at each time t. Consistent with the available information on the individual rate constants for CO:NaCl, but applicable to monolayers on other surfaces if pooling occurs, we assume that the multi phonon relaxation by energy transfer to the solid is slower than the single-phonon-mediated pooling equilibration, so we treat the deactivation separately, as in Section 1.3. The number of sites M and the total number of quanta $N(t)$ in the system (the adsorbed CO) can be expressed in terms of the occupation numbers m_n of each site as:

$$M = \sum_n m_n(t) \tag{1.1}$$

$$N(t) = \sum_n n m_n(t) \tag{1.2}$$

$$F(t) = E(t) - TS(t) = \sum_n m_n(t)\epsilon_n - kTln\frac{M!}{\prod_n m_n(t)!} \tag{1.3}$$

where E is the total vibrational energy at time t, ϵ_n is the energy of the n-th vibrational state of an adsorbed molecule, $S(t)$ is the entropy of the adsorbate, $F(t)$ is the free energy, and $S = klnW$, where W is the number of ways of distributing the N quanta among the adsorbed molecules. For the purposes of simplicity, given the long timescales of the relaxation in question, we consider primarily an after laser excitation picture, where quanta are initially distributed according to the absorbed fluence in the calculations.

We minimize F subject to constraints on total M and N above, apply Stirling's formula to the factorials, introduce a Lagrangian multiplier $\gamma(t)$ and obtain:

$$\frac{m_n(t)}{M} = \frac{e^{\gamma(t)n - \frac{\epsilon_n}{kT}}}{\sum_n e^{\gamma(t)n - \frac{\epsilon_n}{kT}}} \tag{1.4}$$

Phenomenologically, we note that inversion occurs when the energy change for additional pooling requires additional phonon excitation of the solid that exceeds the Debye peak discontinuity in phonon density of states of the solid. We thereby assume that the vibrational number domain for pooling is restricted by (units $\hbar = 1$):

$$\omega_D \geq \epsilon_{1,0} - \epsilon_{n_{max}, n_{max}-1} \tag{1.5}$$

where n_{max} is the maximum integer n attainable energetically by a one-quantum transfer from an

$n = 1$ neighbor by pooling, and so satisfies Eq. 1.5. The pooling maximum arises because of the discontinuity in the density of states at the Debye frequency ω_D (223 cm^{-1}) where in Eq. 1.5, $\epsilon_{n,m} = \epsilon_n - \epsilon_m$, with ϵ_n, the vibrational energy of the oscillator, in this case the adsorbed diatomic molecule, given by:

$$\epsilon_n = \omega_e(n + \frac{1}{2}) - \omega_e\chi_e(n + \frac{1}{2})^2 \tag{1.6}$$

Here, $\omega_e\chi_e = 11.5$ cm^{-1} is the anharmonicity and $\omega_e = 2130$ cm^{-1}, known from CO infrared spectra. In virtue of Eq. 1.5, we restrict the domain to $[0, n_{max}]$.

We rewrite Eq. 1.4 as:

$$ln(m_n) + \frac{E_n}{kT} = \gamma n + ln(M) \tag{1.7}$$

We note that if $ln(P_n) + E_n/kT$ is a linear function of n, then the slope is γ, the only parameter in our distribution.

We can test Eq. 1.7 by comparing with kinetic Monte Carlo results on the ms experimental timescale (the reference[1] gives further details of the calculation). The result is seen in Fig. 1.1 and is evidence of the usefulness of the theory in the present chapter for the constrained distribution of vibrational quanta among the quantum states of the oscillator. The distribution given by Eq. 1.4 is not exact. Nevertheless the results demonstrate that it is a useful description of the inverted distribution with its cutoff at n=10.

The γ appearing in Eq. 4 can be evaluated independently from the following:

$$\frac{N}{M} = \frac{\sum n e^{\gamma n - \frac{\epsilon_n}{kT}}}{\sum e^{\gamma n - \frac{\epsilon_n}{kT}}} \tag{1.8}$$

A simple way of obtaining γ from the value of N/M is to evaluate the right hand side of this function for varied γ, and then find the γ corresponding to the experimentally known N/M. Given an absorption rate constant from lasing of $k_{abs} = 9.0$ x 10^{-4}, one expects a long term excitation of $N/M = (1 - exp(-k_{abs}\tau))/2 = 0.18$ for the lasing duration τ.[2] From this value for N/M, we find $\gamma = 130$, agreeing to every significant figure with the result derived from kinetic Monte Carlo P_n, as shown in Fig. 1.2.

1.3 Resulting Dynamics

The dynamics in the Monte Carlo Simulations are quite complex,[10;9;1] in containing hundreds of first-order and second-order reactions, but can be treated as having to an effective single exponential decay when there is a rapid equilibration process among the states n as follows. Consider the average

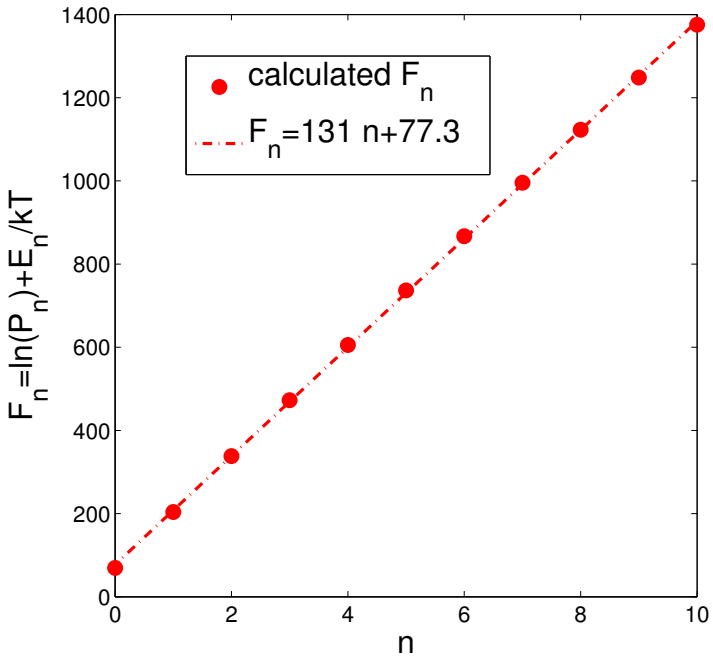

Figure 1.1: The fit for the parameter, γ. The representative pool is derived from monolayer populations, calculated elsewhere by kinetic Monte Carlo,[1] as the slope of $ln(P_n) + E_n/kT$, vs. n, the vibrational state. For the P_n calculated near the end of a pulse of the conditions of the previous monolayer experiment,[2] $\gamma = 131$.

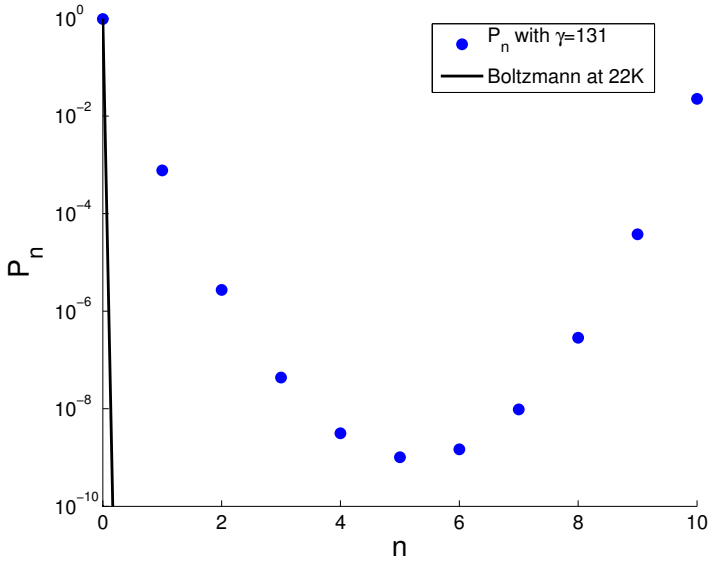

Figure 1.2: This figure shows the P_n from Eq. 1.4 compared to the Boltzmann distribution at 22K for $\gamma = 131$.

number of quanta in any one site:

$$N = \sum nm_n \tag{1.9}$$

In the loss of N vibrational quanta from the pooled surface, the non-radiative excitation of phonons in the solid involves many phonons, and is slow relative to single-quantum pooling equilibration: the latter involves only single excitations, whereas the former involves many such excitations simultaneously. The slow disappearance of quanta in the adsorbate is given by:

$$-\frac{dN}{dt} = \sum \kappa_n m_n \tag{1.10}$$

If there is at each time t a rapid equilibration among the quanta in the adsorbate, then there is a single exponential decay of N, $N = N_0 e^{-\lambda t}$ and $m_n = m_{n_0} e^{-\lambda t}$, so from Eq. 1.9 we have $dN/dt = -\lambda \sum nm_n$. We note that this temporal dependence of the m_n, under rapid pooling equilibration, leads to the same, single-exponential, temporal decay of all states equilibrated, with time constant $1/\lambda$, in contrast to prior expectations for pooling on the H:Si(111) surface.[4]

Comparing with Eq. 1.10, we then have:

$$\lambda = \frac{\sum \kappa_n m_n}{\sum nm_n} \tag{1.11}$$

When applied to the present problem,[1] this model with the theoretical constrained equilibrium distribution given in Eq. 2.10 recovers a reasonably close time constant (3.6 ms for the present theoretical result of Eq. 1.11 vs. 4.3 ms in the full Monte Carlo calculation and experimentally) and single exponential behavior for each state in the pool with the same time constant. We can compare the effective single exponential decay rate with the actual computed results for the monolayer, as in Fig. 1.3.

1.4 Discussion

The consequences of a novel regime of distribution of the vibrational quanta among the different vibrational states are several-fold.[14;13] We note the unifying simplicity of application of the model for different surfaces and phases. While our CO:NaCl(100) simulations at several laser intensities is a time-consuming calculation,[1] the simplicity of the present approximate analytical distribution, when valid, allows one to describe readily other results that may occur experimentally.

We note that the single exponential decay for individual states calculated in this work and elsewhere[9;10;1] indicates that a single exponential decay of individual states cannot be taken as evidence against vibrational pooling, as has been suggested for the H:Si(111) surface.[4] Single exponential de-

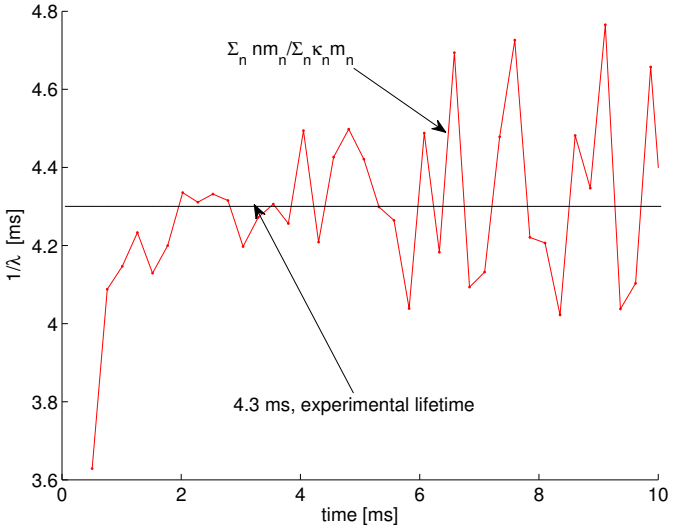

Figure 1.3: Calculated $1/\lambda(t)$ versus time, compared with the single exponential observation.

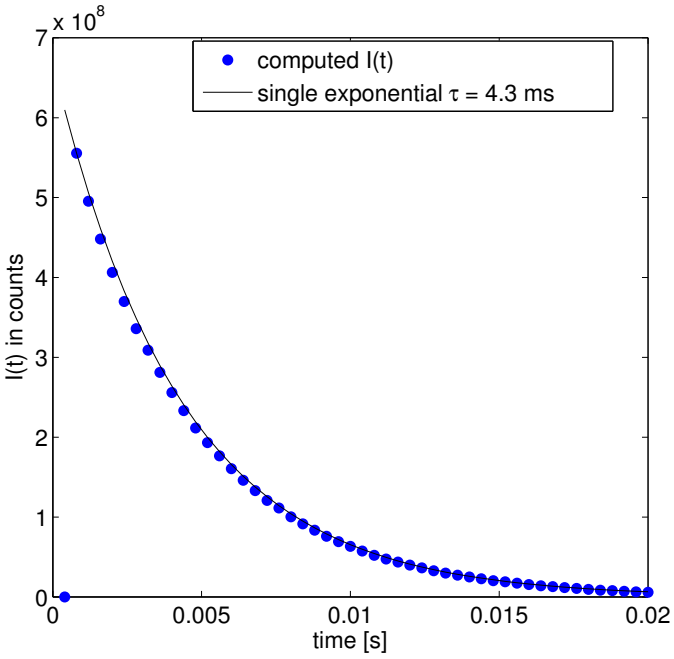

Figure 1.4: The total overtone fluorescence decay (circles computed) matches experiment (solid single exponential with τ=4.3 ms).

cay, even of individual states as observed experimentally (see the discussion preceding Eq. 1.11), does not rule out pooling of the vibrational excitation as long as the latter is rapid relative to the decay to the solid, and this point plays a major role when considering fast bimolecular vibrational processes such as single-quantum assisted non-resonant energy transfer. The key to a single exponential is the validity of the approximation of rapid equilibration between the quantum states of CO molecules on the surface. For example, if a particular state n' has a relatively rapid decay rate by energy loss to the solid (still slow relative to the pooling equilibration, but fast relative to all other processes), the other n s rapidly refill the n' population, so that all states n decay at the same rate. In summary, rapid equilibration among the states relative to loss of quanta to the solid is the key to understanding the single-exponential decay observed both in the experiment and in the computations.

A comparison of the present derivation (CO on a solid) with Treanor's[13] (CO in a gas) is interesting. The N-conservation step is crucial in both, and, up to our Debye-based cut-off, the resulting distribution function is of the same form for both (Treanor's Eq. 4.8 and our Eq. 2.10). In our case, there is a restriction of domain of allowed n-states in the single-quantum exchange with the solid, whereas in the gas phase the non-resonant transfer was aided by a smooth translational energy distribution. However, another difference, purely technical, rather than physical, is in the minimization of free energy in our derivation, as opposed to an entropy-maximization and a temperature ansatz for β in Treanor's. The latter ansatz requires further steps to be made rigorous, namely a calculation of the energy E, entropy S, and an introduction of temperature, $1/T = dS/dE$, to reach a rigorous result, a result obtained simply by a free energy minimization as above.

Of particular interest in the present study is the inverted nature of the distribution, with a maximum at some $n_{max} = \lceil \omega_D/2\omega_e\chi_e \rceil$ following a period of excitation. We note that this limit is proportional to the Debye cutoff frequency and inversely proportional to the anharmonicity, so n_{max} for CO:Si(100) would be 20 because ω_D=448 cm^{-1} for Si(100),[15] assuming the same anharmonicity for CO, while for H:Si(111) it would be 5, since $2\omega_e\chi_e$ = 90 cm^{-1} for that surface, assuming the same ω_D as Si(100). Additional investigation of these surfaces using kinetic Monte Carlo and treating several experimental results[4;16] is the topic of forthcoming work. Pooling equilibration, while minimizing the free energy, also conserves the total number of quanta. Because of this constraint, the population tends to lower its energy by occupying the highest vibrational states, and so inversion is thermodynamically allowed, consistent with a constrained equilibrium statistical mechanics. Complete decay, radiatively and non-radiatively, will occur to eventually yield a thermal equilibrium population distribution, largely in the $n = 0$ state.

The present approximation is not restricted to phonon relaxation of high frequency vibrations on solids, but is relevant in other situations that conserve N, the total number of vibrational quanta, namely: situations where there is rapid single-quantum non-resonant vibrational transfer, faster

than dissipative processes. In all cases, there is then superimposed on these rapid exchanges the slow decay of N. The theory may be extended to treat isolated molecules in matrix solids,[17] and multilayers of CO on NaCl(100).[11;12]

The validity of the equilibration approximation depends on the absorbed laser intensity. It may be expected to be valid when the intensity is sufficiently high. The argument is as follows: equilibration is valid when the decay rate for loss of quanta to the solid is small relative to the rates of the pooling and depooling processes. Pooling is a second-order process and proportional to the square of the light intensity. If the absorbed intensity is too low, the rate of realized pooling will be too slow and the approximation fails.

Quantitatively, for monolayer CO:NaCl(100), where the observed fluorescence relaxation lifetime is 4.3 ms, the calculated rate constant for the 1+ 9 to 0 + 10 pooling reaction is 5 x 10^7 s^{-1} from the kinetic Monte Carlo calculations.[1;10] For this case, wee see that the pooling rate constant, k_{pool} is 2 x 10^5 times faster than the rate of loss of single quanta to the solid, $\lambda \approx 1/(4.3ms)$ (noting again slight variation around this mean lifetime over time as in Fig. 1.3). If $k_{pool}P_1P_9 >> \lambda P_9$, we expect the equilibration condition to be satisfied when $P_1 >> \lambda/(k_{pool}) \approx 5$ x 10^{-6}. Knowing or estimating the cross-section for the absorption and a lifetime for the loss, from $n = 1$ to $n = 0$, for quanta to the solid, one can estimate what laser intensity is needed to obtain any P_1.

In the case of possible vibrational pooling in H:Si(111) Sum Frequency Generation (SFG) pump-probe experiments, there was observed single exponential decay of the $n = 1$ state.[4] There was also observed a hot band,[16] whose observed lifetime is the same as that for recovery of the fundamental at room temperature, 0.9 ns. If the rapid equilibration (fast-pooling) approximation holds, then all $0 < n \leq n_{max}$ should have the same single-exponential rate of relaxation, identical to the rate of $n = 0$ recovery. If there were no equilibration, the lifetimes for $n = 1$ and $n = 2$ would be quite different. For example, computations[18] for a Bloch-Redfield dynamics gave an intrinsic lifetime for the $n = 2$ state of 0.13 ns, and for the $n = 1$ state, 0.9 ns. From previous calculations of the pooling rate constant,[19] the rate constant for the 1 + 1 to 0 + 2 pooling reaction can be as high as $\approx$ 2 x 10^8 s^{-1} on H:Si(111) under some experimental conditions.[4;16] Based on the trends in pooling rate constants for CO:NaCl(100),[1] we expect the pooling rate constant for the $1 + n_{max} - 1$ to $0 + n_{max}$ pooling reaction, k_{pool}^{SiH}, to be 7 x 10^9 s^{-1}. In this case, the calculated pooling rate constant is ≈ 10 times the observed rate of loss of single quanta to the solid ($\lambda^{SiH} \approx$1/0.9 ns =1 x 10^9 s^{-1}), and $P_1 >> 0.1$ would meet the equilibrium condition.

One can also examine the spectrally integrated SFG intensity in the previous hot band pump-probe experiment for evidence of pooling on H:Si(111).[16] We calculate that, after pumping, the spectrally integrated SFG intensity is approximately 1/3 the value before pumping (inferred from Fig. 1 of the reference[16]). One possibility for this reduction in integrated signal is that pooling is fast, and much of the excited population is at the pooling maximum (n_{max}=5 for H:Si(111)). In

the previous experiment, following the pump, the SFG probed the 1840-2125 cm^{-1} range.[16] If one extended the SFG probe range to 1600-2125 cm^{-1} following the same pump as before,[16] then it may be possible to see if the majority of the spectrally integrated SFG intensity after pumping occurs at $n = 5$. If fast-pooling occurs, one expects to see the $5 \rightarrow 6$ transition dominate the post-pumping SFG, which is expected to be around 1630 cm^{-1}. We plan to discuss these and other issues[20] for the H:Si(111) system further in a later publication.

1.5 Conclusions

In the present theory, a simple distribution is derived by a free energy minimization during vibrational-quanta-conserving pooling equilibration on solids. In particular, the following experimentally testable predictions are made:

1- Statistical behavior is expected in vibrational equilibria, subject to the constraint of a slowly decaying number of quanta $N(t)$ when the vibrational equilibration is fast relative to all radiative and non-radiative processes. This behavior can be described by the temperature and Debye frequency of the solid along with the anharmonicity and fundamental frequency of the high frequency vibration.

2- All vibrational populations on surfaces in this model are described by restricting quantum state n to the domain $[0, \lceil \omega_D / 2\omega_e\chi_e \rceil]$. The vibrational pools are coupled by all resonances and near-resonances consistent with the preservation of the number of quanta.

3- Temporal single-exponential decay cannot be taken as evidence against vibrational pooling despite the bimolecular rate constant behavior of individual rates and the unimolecular dependence of other steps. Indeed, single exponential decay is the expected result if pooling equilibration is faster than all decay processes.

Chapter 2

On the Infrared Fluorescence of Monolayer ^{13}CO:NaCl(100)

2.1 Introduction

Carbon monoxide (CO) on an NaCl(100) surface has been used as a model system for surface vibrational excitation since around 1990.[21;22;11;12;2] Several low temperature experiments have been conducted on monolayers and multilayers of ^{12}CO and ^{13}CO, observing overtone ($n + 2 \rightarrow n$) infrared fluorescence from monolayer ^{13}CO excitation between the 2nd and 16th vibrational state[2] and multilayer ^{13}CO excitation reaching the 30th vibrational state.[11;12] In the monolayer case, these states were inferred by application of a filter (4200 - 3400 cm^{-1} transmitted) to the total integrated overtone emission, and in the multilayer case these states were observed directly by the collection of dispersed fluorescence.

Ewing et al.[2] suggested that the mechanism for this localization of vibrational energy may be the energetically favored vibrational pooling reaction, where a pair of Morse-like oscillator neighbors non-resonantly transfer a vibrational quantum in a step that is exothermic due to the anharmonicity. This vibrational energy transfer can in principle occur with sites further removed than nearest-neighbors, but as a first approximation we focus on nearest-neighbor and single vibrational quantum exchanges.

The present formulation builds on a model of pooling and depooling rate constants given by Corcelli and Tully for this system and this surface.[9;10] We also use the same Kinetic Monte Carlo (KMC) algorithm to evaluate the vibrational population evolution.[9;10] We extend their pioneering work to larger grid sizes (10,000 sites instead of 256), higher vibrational states ($n = 45$ instead of $n = 15 - 20$), and to higher fluence laser conditions, including stimulated emission. Additionally, we test our previous theoretical prediction of the explicit form of the constrained vibrational population distribution function.[1] In it, the n- domain of a pool is restricted by the maximum energy that can be dissipated by pooling exchanges exciting only single-phonons in the solid.

2.2 Vibrational Exchange for monolayer CO

In a resonant vibrational exchange, the vibrational energy of the pair of neighbors is conserved in the energy transfer, whereas in a non-resonant exchange, some of the energy excites or removes phonons from the solid. This non-resonant case provides both a ladder-climbing mechanism for vibrational excitation and a ladder-descending pathway for vibrational relaxation of the energy difference in the transition. This pooling-depooling effect is described for a vibrational state n in the following equations:

$$|n\rangle + |m\rangle \overset{W^p_{n,m}}{\longrightarrow} |n+1\rangle + |m-1\rangle \tag{2.1}$$

$$|n+1\rangle + |m-1\rangle \overset{W^d_{n+1,m-1}}{\longrightarrow} |n\rangle + |m\rangle \tag{2.2}$$

where the $W^p_{n,m}$ are pooling rate constants for a site in state n receiving a single vibrational quantum of energy from a neighboring CO site initially in state m, and the reverse reaction is described by a depooling rate constant $W^d_{n+1,m-1}$.

We treat the effect of pooling on the time-evolution of $P_n(t)$, the probability of a single site being in the n^{th} vibrational state at time t, where n is the specific vibrational level whose time-evolution is being described. We have:

$$\sum_{n=0}^{\infty} P_n = 1 \tag{2.3}$$

noting that, in the present model, every site is occupied and thus is in some CO vibrational state, $n = 0$ and upward. Adsorption and desorption of CO are not considered, since the experimentally observed dissociation rate is slower than $10^{-4}s^{-1}$ at 22 K,[23] and so should not be observed on the 20 ms experimental timescale, being 6 orders of magnitude slower.[2] All simulations are at 22 K, the temperature of the experiments.[2;11;12]

We define $(dP_n/dt)_{pd}$ as the net rate of pooling and depooling of state n with nearest neighbors. The pooling and depooling terms are described in Eqs. 1 and 2 in terms of the effect on a specific vibrational state n:

$$\begin{aligned}\frac{dP_n}{dt}_{pd} = &\sum_m (W^p_{n-1,m})P_{n-1,m} + \sum_m (W^d_{n+1,m})P_{n+1,m} \\ &- \sum_m (W^p_{n,m})P_{n,m} - \sum_m (W^d_{n,m})P_{n,m}\end{aligned} \tag{2.4}$$

where $P_{n,m}$ denotes the joint probability that there is a site in a vibrational state n and that there is an adjacent site having m quanta (such that $\sum_m P_{n,m} = 4P_n$, since every site has 4 neighbors). Adding relaxation steps to the above, by energy loss to the solid on which the CO is adsorbed, the

vibrational state probability evolution of a site on a CO surface is:

$$\frac{dP_n}{dt}_{pdrf} = \frac{dP_n}{dt}_{p-d} - \kappa_n P_n + \kappa_{n+1} P_{n+1} \tag{2.5}$$

where the κ_n denote the relaxation rate constants for transfer of energy to multiphonons in the solid. The formulae for the relevant rate constants are given in Chapter Appendix A. A comparison of the resulting rate constants of pooling, depooling, and relaxation along with fluorescence and overtone fluorescence is given for many n's in Figs. 2.1 (a) and (b).

These equations are used for $1 < n < 45$, with a closure introduced into the equation for $n = 45$ in Eq 2.4 by making transfer to P_{46} impossible ($P_{46} = 0$). The vibrational populations $P_n(t)$ can then be obtained by kinetic Monte Carlo integration[24] of all possible rates, as discussed by Corcelli and Tully[10] and references cited therein, using site-to-site surface hopping methods for the energy transfer.

To allow the intensity of incoming light to be treated explicitly, we added to the KMC code terms containing the absorption coefficient $k_{abs,l}$, the Einstein coefficient for each laser, to $(dP_n/dt)_{pdrf}$ in Eq. 2.5. We considered only single-photon excitations from $n = 0$ to the $n = 1$ state:

$$\frac{dP_0}{dt} = -k_{abs,l}(P_0 - P_1) + \frac{dP_0}{dt}_{pdrf} \tag{2.6}$$

$$\frac{dP_1}{dt} = k_{abs,l}(P_0 - P_1) + \frac{dP_1}{dt}_{pdrf} \tag{2.7}$$

where the $(dP_n/dt)_{pdrf}$ are calculated as in Eq. (2.5) above, and $k_{abs,Mono} = I\sigma/(\hbar\omega)$ is calculated to be 9 x $10^4 s^{-1}$ for monolayer laser conditions, 25 μJ in 5 μs, σ = 3 x 10^{-17}cm^{2}molecule^{-1}.[2] To examine populations under lasing by higher fluence sources, we also examined excitation by the CLIO Free Electron Laser (FEL) by following a single averaged macropulse, $k_{abs,CLIO} = 5$ x $10^7 s^{-1}$, from 20 mJ in 8 μs.[25] We note that, for higher fluence lasers, one must include both stimulated absorption and emission.

Given that the rate of overtone fluorescence is slower than the energy transfer from the n state to multiple phonons in the solid, the total overtone fluorescence intensity at time t, $I(t)$, is given by:

$$I(t) = \frac{N_{sim}}{A} \sum_n k_f^{\Delta v=2} P_n(t) = \sum_n I_n(t) \tag{2.8}$$

where $I_n(t) = (N_{sim}/A) k_f^{\Delta v=2} P_n(t)$ and there are $N_{sim} = 10^4$ sites per trajectory, representing a surface area $A = 1.57$ x 10^{-11} cm^2 as in Corcelli and Tully.[9] Resonant diffusion out of the illuminated spot is not considered.

The total dispersed overtone fluorescence, $S(\omega)$, is obtained by integration of the fluorescence

intensity over a time τ_i, the overtone fluorescence lines summed over all wavelengths:

$$S(\omega) = \sum_{n=2}^{45} L_n \int_0^{\tau_i} I_n(t) dt \tag{2.9}$$

with the integrals approximated trapezoidally given $P_n(t)$ and t from the program output up to integration time τ_i. The times τ_i are chosen to represent different length fluorescence collection experiments. L_n is the line shape, approximated for each line as a normalized Gaussian with FWHM 10 cm^{-1}. This lineshape is preferred over the Lorentzian by a fit to the experimental dispersed overtone fluorescence emission from multilayers of CO on NaCl(100), for each overtone line, at the same temperature as the monolayer experiment.[26;11] Snapshots of Eq. 2.9 are also given.

We study the ^{13}CO monolayer rather than a ^{12}CO system following the experimental work of Ewing et al.[2;11;12] and the simulation of Corcelli and Tully[9;10]. This isotope was chosen for the experiments to enhance the overlap of its fundamental frequency with the ^{12}CO gas laser emission.[27]

Following Corcelli and Tully,[9;10] the relaxation rate constants (κ_n) are found by introducing a system-bath coupling scale parameter λ which multiplies the Debye density of states as a rough estimate of the strength of coupling between surface oscillators and bath, and fixed such that the experimentally observed total overtone fluorescence lifetime (4.3 ms) is recovered under monolayer conditions. We find a single exponential decay matching the experimental observations, as in Fig. 2.2, for $\lambda = 0.470$, close to the value of Corcelli and Tully ($\lambda_{CT} = 0.522$), and similar relaxation rates of $\kappa_1 = 6.7s^{-1}$ compared to 5.7 s^{-1} in the previous simulation. We find different rates in the present calculation primarily because we use the experimental decay of overtone fluorescence to fix the calculated effective decay rate of overtone fluorescence, whereas the previous simulation appears to have matched the computed fundamental fluorescence decay to the experimental overtone fluorescence results.[9;10;2]

2.3 Kinetic Monte Carlo Results

We first analyze the total overtone fluorescence in Fig. 2.2 which has been fit via the system-bath coupling parameter λ. The calculated vibrational populations at the end of each laser-on period and 1 ms thereafter are compared in Figs. 2.3 and 2.4, respectively. We confirm that for the monolayer, the overtone fluorescence results primarily from n=8 − 10, as previously calculated.[9;10]

We also confirm in the computations the theoretically predicted distribution function derived in another work,[1] as in Fig. 2.5. Shown is the deviation that is linear in n, a deviation from the Boltzmann distribution across the one-phonon domain restricted regime, with slope $\gamma = 131$. We discuss this result further in the next section.

The signal calculated in Figs. 2.6 and 2.7 is given is in total photons cm^{-2}. The signal in Fig.

Table 2.1: The calculation times and results for a single trajectory on a 100x100 grid with three different resonant rate conditions 1ms following monolayer excitation. They each have relative peaks at $n = 10$, not shown.

resonant rate factor	computational time (min.)	P_{10}(1 ms)
1/1000	9	0.0196
1/100	91	0.0206
1/10	1179	0.0182

2.8 is integrated over a short time relative to the full time of simulation. These times are effectively snapshots since the small timescale of the observation is ms. The timescale of the snapshot is varied between simulations, but the integration is not converged: since fluorescence is ongoing from changing populations, the timescales of integration are representative of experimental binning effects, given fixed bin sizes for collecting fluorescence ranging from $\approx 1 - 10$ μs.

To understand further the evolution of the vibrational excitation of the CO molecules on the surface, we have examined representative snapshots from a single trajectory at the end of the first laser pulse and 1 ms thereafter in the high energy case in Figs. 2.9.

The results for the $P_n(t)$ are robust to grid size, since 10 trajectories on a 100 x 100 surface give results for the $P_n(t)$ that are indistinguishable from those obtained from 1 trajectory on a 300x300 grid after 1 ms for monolayer excitation conditions. The two sets of trajectories have roughly the same implied maximum resolution in $P_n(t)$, namely $N_{traj}^{-1} N_{sites}^{-1} = 10^{-5}$ vs. (1/9)x10^{-4}. The results are also robust with respect to variation of the resonant transfer rate constant, which is reduced by three orders of magnitude to realize similar order gains in computational time. Increasing the resonant rate constant by two orders of magnitude showed no noticeable change in the results for the P_n distribution obtained for monolayer fluence conditions calculated at 1ms, except for the significant additional computational time, as seen in Table 2.1.

While the results show pronounced maxima based on the effect of the single-phonon Debye cutoff (peaks around $n = 10$, 19 and 27 in the figures), the results including two-phonon assisted rates were indistinguishable from those including only single-phonon transfers. This is not surprising, since the two-phonon rates are expected to be significantly slower, as in Fig. 2.1.

2.4 Discussion

The present computational results agree with those in the previous simulation[9;10] on this CO/NaCl(100) surface in finding a vibrational pooling peak around the n=10 state on the ms timescale. The monolayer excitation condition in Fig. 2.3 and 2.4 can be compared directly with Figs. 3 a and b in the reference,[10] finding the peak around $n = 10$ and similar trends on both sides of the peak.

We have described in a previous work[1] (Chapter 1) a statistical theory of the distribution function under conditions of relatively low excitation,based on the condition imposed by one quantum assisted

emission in pooling, limited by the Debye frequency, $\hbar\omega_D$ of the solid. The distribution function as derived in the reference,[1] is given by:

$$P_n(t) = \frac{m_n(t)}{M(t)} = \frac{e^{\gamma(t)n - \frac{\epsilon_n}{kT}}}{\sum_n e^{\gamma(t)n - \frac{\epsilon_n}{kT}}} \tag{2.10}$$

In this approximation, while in the domain of change of n by energy transfer accompanied by one-phonon pooling, the P_n are primarily constrained in the interval $[0, 10]$. Clearly this constraint on n does not hold for the CLIO excitation at short times, as in Fig. 2.3, but by 1 ms the assumption appears to hold reasonably well for both lasing conditions, as in Fig. 2.4. As a result, we are able to confirm in Fig. 2.5 that the constrained statistical theory described in the previous Chapter[1] is in agreement with the presently calculated dependence on n. The systematic deviation from the Boltzmann expectation with n is as theoretically expected in Eq. 2.10:[1] γ is the slope of $F_n = ln(P_n) + E_n/kT$, vs. n, the vibrational state. If there is no component of the Free Energy (F_n) which is dependent on n, then there should not be a dependence.

Using higher laser fluences than before and examining populations during the duration of lasing, we have found substantial populations of many $n > 16$ states, as in in Fig. 2.3, including evidence of strong inversion near the $n = 22$ state ($3.5\text{x}10^{10} photons\ cm^{-2}$ after 1 ms of collection, as in Fig. 2.7). By extending earlier work to higher intensities, these high lying states have been calculated to exist in significant populations on this surface, and they result from the complex interplay of rates, some of which are given in Fig. 2.1. Experimentally, levels as high as the $n = 26$ state were inferred to have been observed in the dispersed fluorescence of multilayers of $^{13}C^{18}O$.[11] The extent of the observability of higher states experimentally depends on the temporal resolution of the apparatus. To our knowledge there have been no further experiments on the CO:NaCl(100) system since 1990, and none with a higher fluence free electron laser source of the sort described here. These calculations have spawned the related theory, and remain an important first step.

As seen in Figs. 2.6 and 2.7 after 1 ms following excitation, the distribution is more narrowly peaked around an $n = 10$ maximum at lower fluences, and becomes broader and peaked around slightly higher values at higher fluences. Over time, the evolution of pools by relaxation leads to a characteristic dispersed fluorescence signature, calculated by Eq. 2.9.

For all the systems with high levels of excitation, as in Figs. 2.9, one notices immediately a checkerboard pattern as a result of competition between different sites for the accumulation of quanta. When excitation levels are somewhat lower, as in the snapshots 1 ms following excitation, this competition is limited to single-phonon-assisted transfer rates, which are much faster than multi-phonon-assisted transfer. This pattern is identified as an anti correlation between pooling peak states ($n > 1$, but typically n = 8,9 or 10) or correlations between peaks and vacancies, and it occurs within 2 microseconds after excitation, remaining anti correlated throughout all of our

simulations, as long as the pool states exist (four orders of magnitude in time). As a result, the mean-field approximation of the master equation is not expected to give accurate results.

We include stimulated emission in these calculations for the first time. We suggest that the previous experiments could not measure fluorescence (instead measuring the overtone) because of the overwhelming stimulated emission signal during lasing. While arising from the much faster stimulated emission process (k_{abs} = 9 x 10^4 s^{-1}), the photons collected would be indistinguishable from fluorescence ($k_f^{\Delta v=1} = 11.4 s^{-1}$). This effect also adds many more Monte Carlo steps to the calculation at the higher lasing fluence, more than doubling the computational time required.

It may appear at first unusual that, over time, the populations excited by higher intensity lasers relax to similar distributions as those at lower fluence light, since three orders of magnitude of fluence are spanned. This calculated result may be the signature of a constrained statistical behavior in a physically based vibrational energy distribution, as explored theoretically in the previous chapter.[1]

2.5 Conclusions

In the present model, vibrational pooling leads to the accumulation of vibrational energy in ^{13}CO on NaCl(100). The model suggests substantial vibrational population inversion under existing laser conditions.

Importantly, the calculation supports the constrained vibrational population distribution recently derived theoretically for monolayers of high-frequency vibrations at solid surfaces where the assumptions of the model hold.[1] Further theoretical characterization of this high fluence regime, where the previous theoretical assumptions fail, is the topic of ongoing research.

The following experimentally testable predictions are also made:

1- States as high as $n = 32$ may be excited with currently available laser conditions (1.5x10^4photons cm^{-2} 7-8 μs following lasing under CLIO FEL conditions), although the continued brightness of the $n \approx 10$ pooled states through the ms timescale (4x10^{11} photons cm^{-2} after 8 ms as in Fig. 2.7 (b) may restrict the observability of these higher states by dispersed fluorescence.

2- In addition to the inverted distribution with a peak at $n = 10$ persisting to 20 ms, there is predicted to be a second inverted peak in the dispersed overtone fluorescence expected to appear around $n = 22$, 2x10^9photons cm^{-2} after 1 ms of continuous collection, as in Fig. 2.7, when the absorbed laser fluence prior to relaxation lifetime is increased to Free Electron Laser intensity.

2.6 Chapter Appendix A: Rate constants

We use the relaxation rate expression from Corcelli and Tully:[10]

$$\kappa_n = \sum_{p=1}^{\infty} \frac{f_p I_p}{\omega_n p!} |\langle n|x|n-1\rangle|^2 [n(\frac{\omega_n}{p}) + 1]^p \tag{2.11}$$

$$f_p = (-1)^p (2^{p+1} - 2) D' \alpha'^{p+1} \frac{m_O}{M_{CO}}) \tag{2.12}$$

$$I_p = \lambda^p \frac{\omega_n}{\omega_D} \sqrt{\frac{75\pi}{p}} exp[-(\frac{75}{4p})(\frac{\omega_n}{\omega_D} - \frac{4p}{5})^2] \tag{2.13}$$

$$n(\omega) = (e^{\frac{\omega}{kT}} - 1)^{-1} \tag{2.14}$$

where p is the order of phonon excitation of the solid and λ is the only free parameter (in Eq. 8). We note two slight typos in I_p in the original work have been identified (compared to the reference),[10] but there was no corresponding typo in the program. The remaining quantities are the temperature of the solid (22K), the Debye cutoff $\omega_D = 223$ cm^{-1},[10] the energy levels of the CO Morse oscillator ω_n, the mass of oxygen $m_O = 16$ amu, the total mass of CO, $m_{CO} = 29$ amu, and the properties of the Morse coupling of the CO to the NaCl, the binding energy $D' = 0.168$ eV and $\alpha' = 0.816$ Å^{-1}.[10]

To calculate the vibrational pooling rate constants, $W^p_{n,m}$ we use:[9;10]

$$\begin{aligned} W^p_{m,n} = \quad & \textstyle\sum_{p=1}^{\infty} 2\pi p! 2^p g_p^2 |\langle n|x|n-1\rangle|^2 \\ & |\langle m|x|m+1\rangle|^2 [\tfrac{n(\frac{\omega_{n,m}}{p})+1}{M_{Na}}]^p H_p \end{aligned} \tag{2.15}$$

$$g_p = (-1)^p \tfrac{\mu'^2 (p+1)(p+2)}{2R_0^{p+3}} \tag{2.16}$$

$$\begin{aligned} H_p = \quad & \textstyle\int_0^{\infty} \mathrm{d}\omega_1 \cdots \int_0^{\infty} \mathrm{d}\omega_p \, \tfrac{\rho(\omega_1)}{\omega_1} \cdots \tfrac{\rho(\omega_p)}{\omega_p} \\ & \delta(\omega_{m,n} - \omega_1 - \cdots - \omega_p) \end{aligned} \tag{2.17}$$

noting that depooling rates $W^p_{m,n} = W^d_{m+1,n-1} e^{\beta \omega_{n,m}}$ are also known immediately by detailed balance. Besides p, the number of phonons of the solid needed to mediate the transfer, the other parameters are: the energy dissipated by the pooling $\omega_{m,n} = \omega_n - \omega_{m+1}$, the site-to-site distance between nearest neighbor CO molecules $R_0 = 3.96\mathring{A}$, the mass of the Na^+ ion $M_{Na} = 23$ amu, and the normalized phonon density of states $\rho = 3\omega^2/\omega_D^3$ for $\omega < \omega_D = 223$ cm^{-1}, for a Debye solid.[9;10]

The $k_n^{\Delta n=i}$, fluorescence rate constant for a CO with n vibrational energy quanta, are obtained from the standard relations:[28]

$$k_n^{\Delta n=1} = \frac{16\pi^3 \omega_n^3 \mu'^2}{3\epsilon_0 hc^3} |\langle n|x|n-1\rangle|^2 \tag{2.18}$$

$$k_n^{\Delta n=2} = \frac{16\pi^3 \omega_{n\Delta 2}^3 \mu'^2}{3\epsilon_0 hc^3} |\langle n|x|n-2\rangle|^2 \tag{2.19}$$

where $\omega_{n\Delta 2}$ is the frequency of the n to n-2 overtone fluorescence, μ' is the coefficient in the transition dipole moment, $d\mu(x)/dx|_{x=0}$ (1.8D/$\mathring{A}$ in the case of ^{13}CO),[10] and the matrix elements can be evaluated, for example in a Morse oscillator basis. Following Gallas,[29] the Morse oscillator matrix elements are given by:

$$\langle n|x|n-1\rangle = \frac{1}{a(k-2n)}\left(\frac{n(k-2n-1)(k-2n+1)}{(k-n)}\right)^{1/2} \tag{2.20}$$

$$\langle n|x|n-2\rangle = \frac{-1}{2a(k-2n+1)}\left(\frac{n(n-1)(k-2n-1)(k-2n+3)}{(k-n+1)(k-n)}\right)^{1/2} \tag{2.21}$$

where the Morse constants are a=2.209 Å^{-1} and D = 12.3 eV and $k = \omega_e/\omega_e\chi_e = 185$, ω_e =2130 cm^{-1} is the fundamental frequency of the Morse oscillator and $\omega_e\chi_e$ = 11.50 cm^{-1} is the anharmonicity (such that ω_2 = 2084 cm^{-1}). The resulting overtone fluorescence rate constants range from $k_2^{\Delta n=2}$ = 0.239 s^{-1} to $k_{44}^{\Delta n=2} = 60.2s^{-1}$. The fundamental fluorescence rate constants range from $k_1^{\Delta n=1} = 11.6s^{-1}$ to $k_{26}^{\Delta n=1} = 135s^{-1}$.

2.7 Chapter Appendix B: Units

To connect with units traditionally used in chemical kinetics, we describe the population evolution equations below, adapting $(dP_n/dt)_{pdrf}$ in Eq. 2.5 to more familiar units. Let M_n be the number of sites that have n quanta. We then have $P_n = M_n/M$. Let $P(m|n)$ be the conditional probability, in particular the probability that given a site with n quanta, there is an adjacent site with m quanta. So in Eq. 2.5 we replace the $P_{n,m}$'s with $P_nP(m|n)$'s. The P_n's replace the normal concentrations c_n in kinetics,

$$\begin{aligned}\frac{dP_n}{dt}_{pd} = &\sum_m (W^p_{n-1,m})P_{n-1}P(m|n-1)+ \\ &\sum_m (W^d_{n+1,m})P(m|n+1)P_{n+1} \\ -\sum_m (W^p_{n,m})P(m|n)P_n &- \sum_m (W^d_{n,m})P(m|n)P_n\end{aligned} \tag{2.22}$$

As a result, the units of the second-order rates are technically per conditional probability of an m neighbor, given an n-site under consideration.

(a)

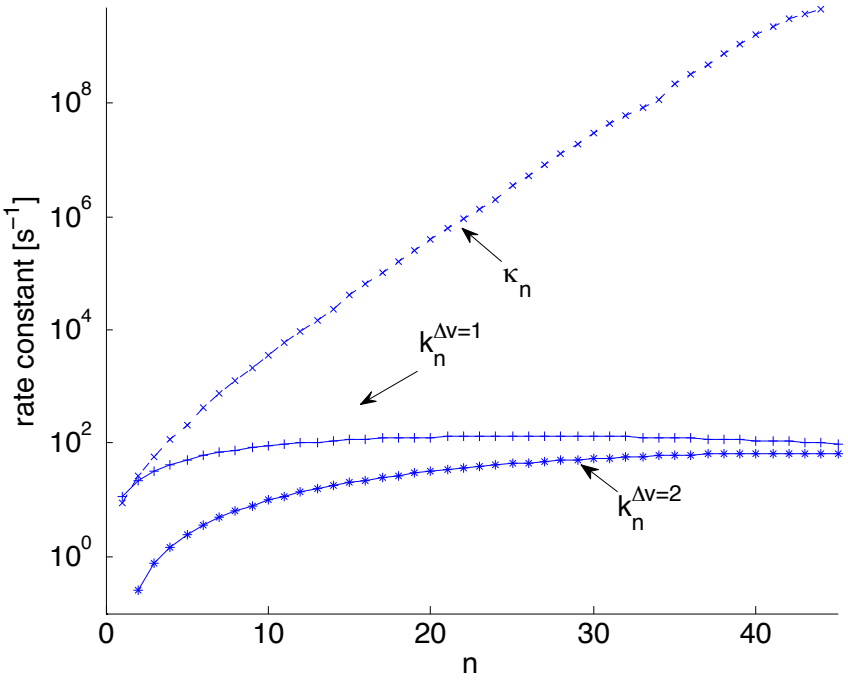

(b)

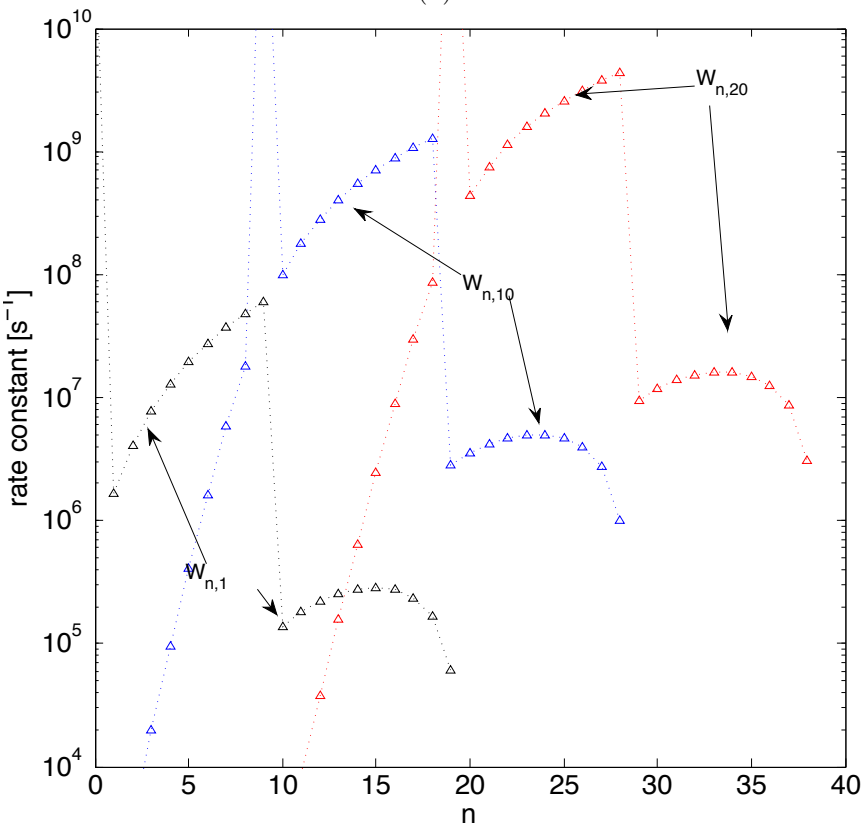

Figure 2.1: Comparison of relevant rate constants: (a) first-order rate constants of relaxation (κ_n), fluorescence ($k_n^{\Delta v=1}$) and overtone fluorescence($k_n^{\Delta v=2}$) (b) second-order rate constants of pooling ($W^p_{n,m}$ for m =1,10 and 20). The second order effect of pooling to state n from an $m = 1$ state which requires an additional phonon to transfer to $n \geq 10$, and so $W^p_{10,1} \approx 10^{-3} W^p_{9,1}$. As second order rate constants, the pooling and depooling rate constants should be multiplied by a conditional probability if one wishes to compare with the first order rate constants, leading to units [s^{-1} per unit conditional probability $P(m|n)$], as discussed in Chapter Appendix B.

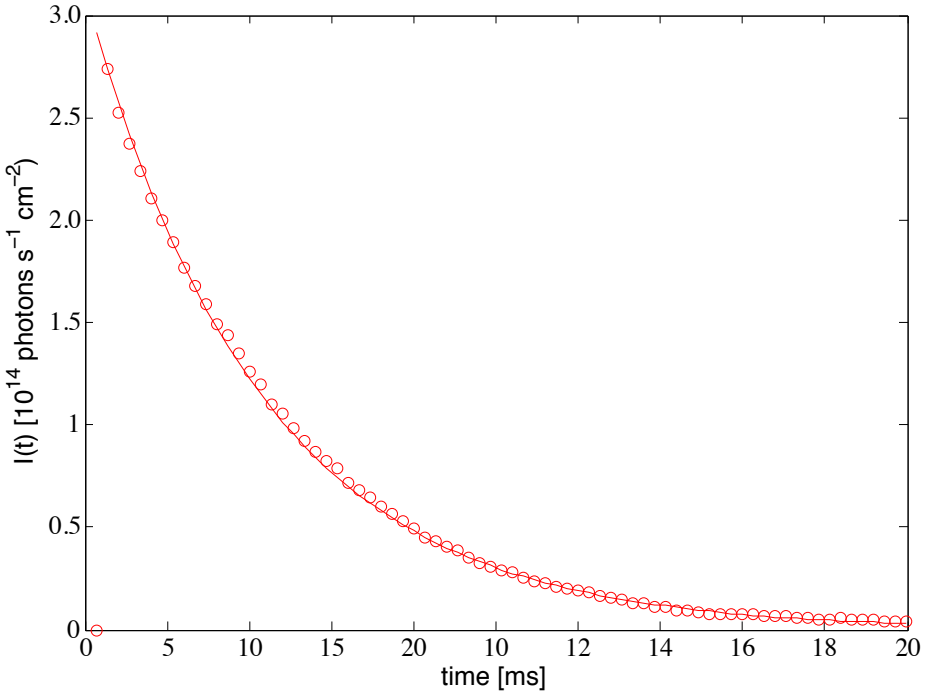

Figure 2.2: The total overtone fluorescence decay (circles computed) matches experiment (solid single exponential, $I(t) = I(0)exp(-t/\tau)$, with time constant τ=4.3 ms).

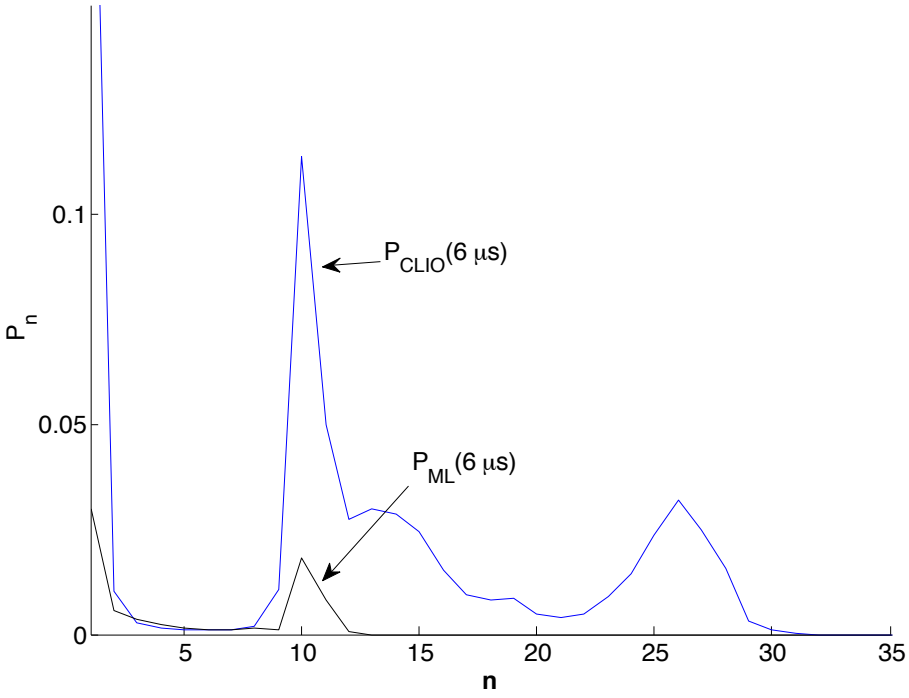

Figure 2.3: The vibrational population 6 μs following beginning of pulse (near end of lasing).

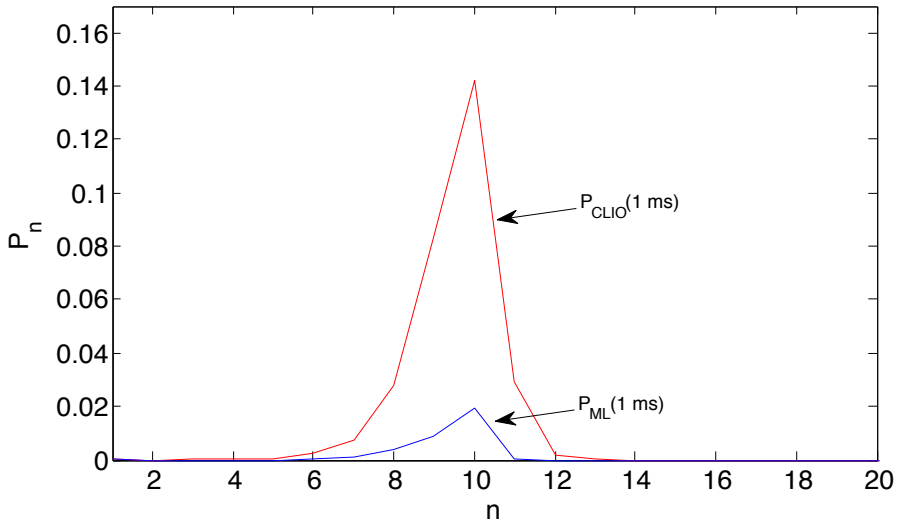

Figure 2.4: The vibrational population 1 ms following the beginning of lasing.

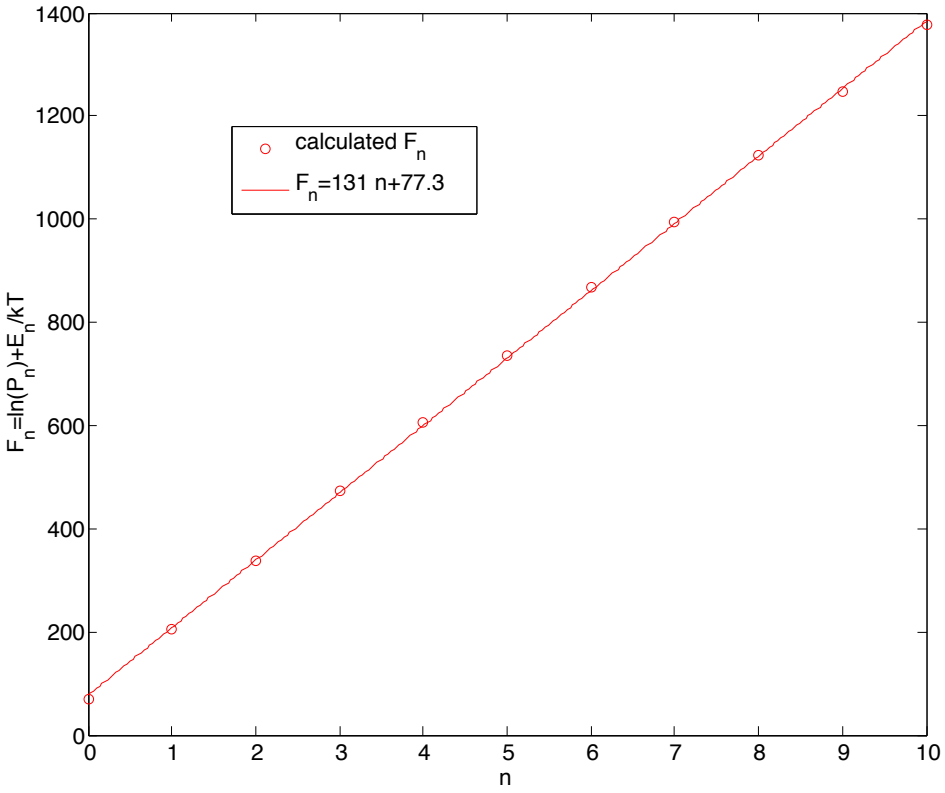

Figure 2.5: The fit of the computed results to the theory-based expression permits the evaluation of statistical parameter $\gamma = 130$, from the slope of the linear fit on the restricted n domain. A typical result for P_n after 4 ms following monolayer excitation is displayed, although this γ is representative of those where the restricted n-domain assumption holds.

(a)

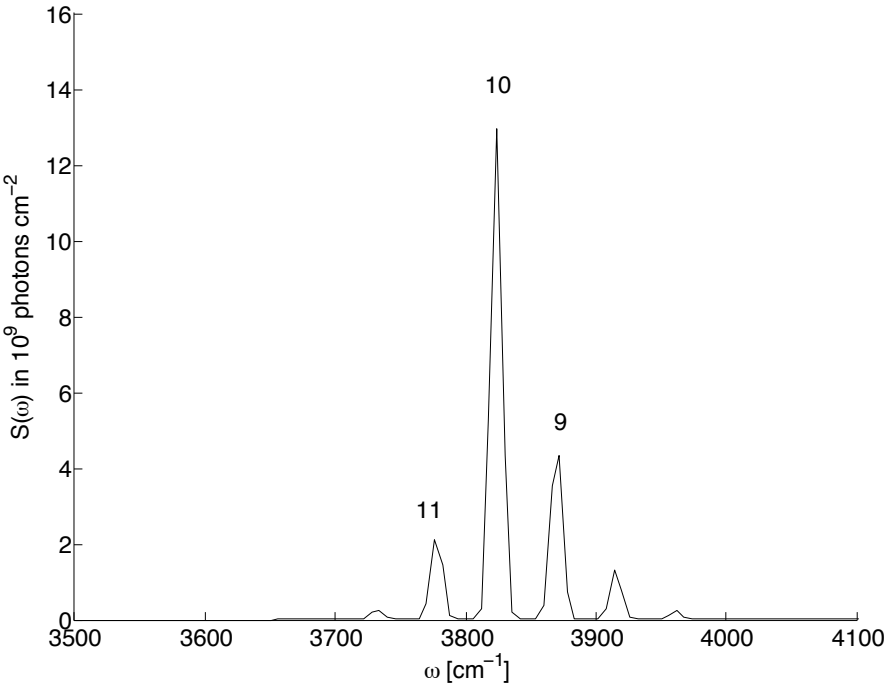

(b)

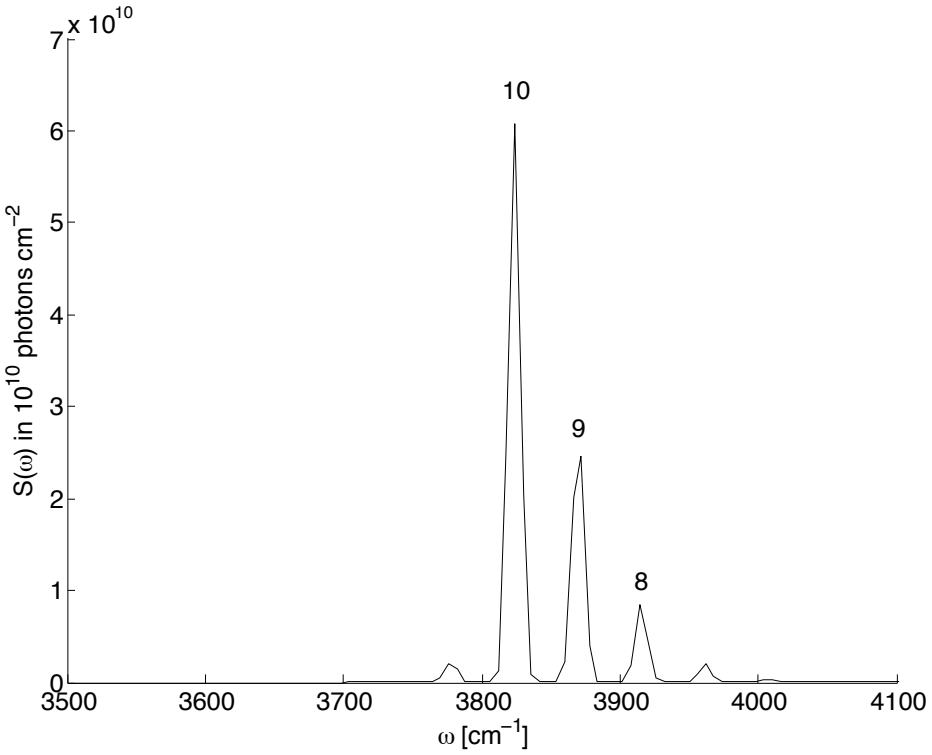

Figure 2.6: The theoretical dispersed fluorescence (assuming perfect collection efficiency) for a monolayer under the experimental monolayer lasing conditions (k_{abs}=9 x $10^4 s^{-1}$), integrated over a (a) 1 ms and (b) 20 ms period after the beginning of lasing.[2] The temporal integration was calculated trapezoidally from $P_n(t)$ at 79 time points spread equally over the length of calculation.

(a)

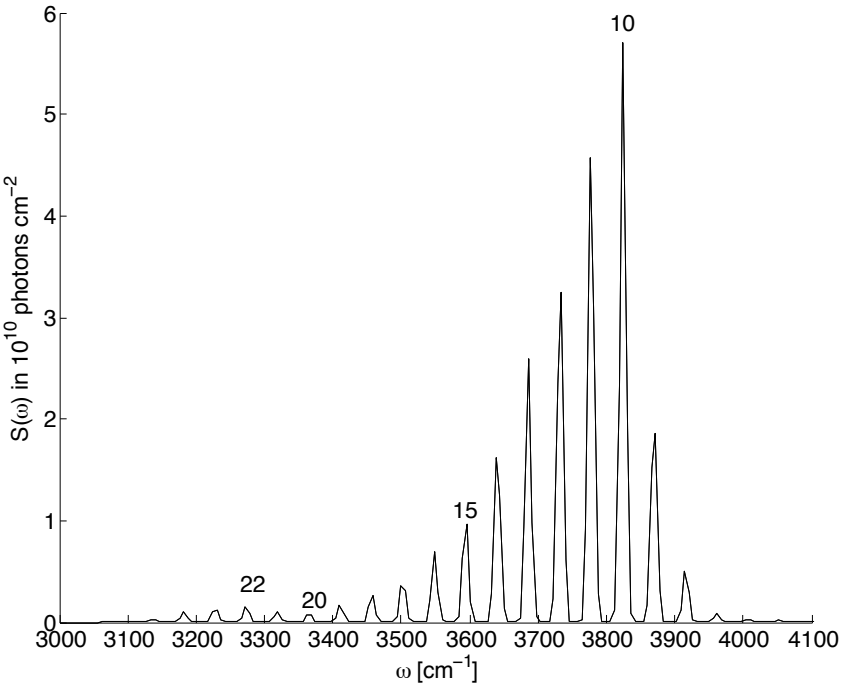

(b)

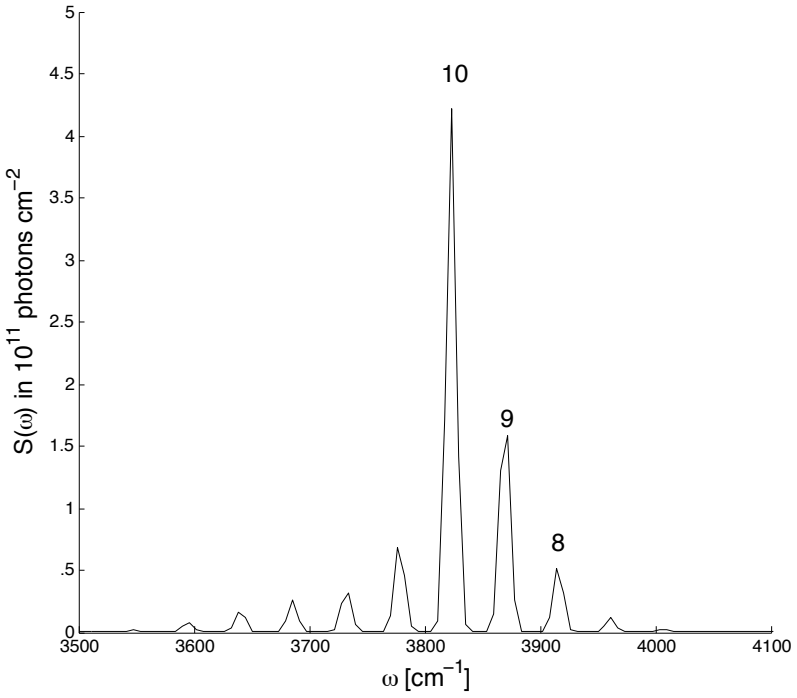

Figure 2.7: The theoretical dispersed fluorescence (assuming perfect collection efficiency) after (a) 1 ms and (b) 8 ms following CLIO excitation of a monolayer (averaged over a macro pulse for the highest fluence currently available at that wavelength, $k_{abs,CLIO} = 5$ x$10^7 s^{-1}$ for 8 μs, or 20 mJ). We note that, in (a), the appearance of a tiny higher n shoulder around $n = 22$ (which is even more pronounced as a relative peak at shorter times, not shown), but that the signal on the ms timescale is overwhelmed by fluorescence from lower n and the distribution becomes the same as that for the monolayer under continued observation.

(a)

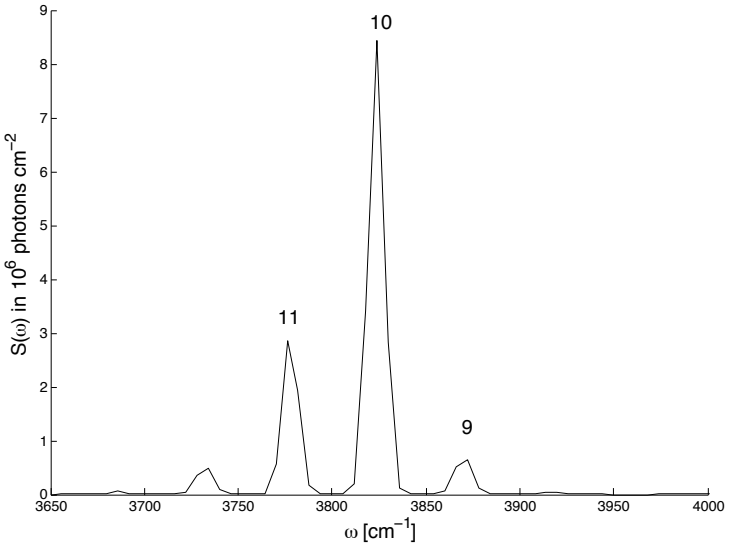

(b)

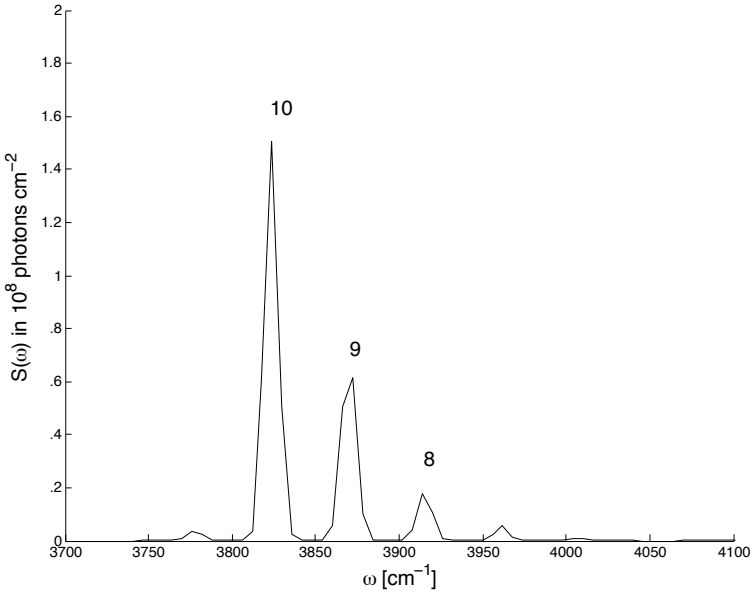

Figure 2.8: Snapshots of the theoretical dispersed fluorescence for a monolayer under the experimental monolayer lasing conditions (k_{abs}=9 x $10^4 s^{-1}$). The snapshots given are (a) 1 μs between 77 and 78 μs following beginning of excitation and (b) 12.7 μs period ending 1 ms after the beginning of lasing, representative of the difference in results at different temporal resolutions of collection.

(a)

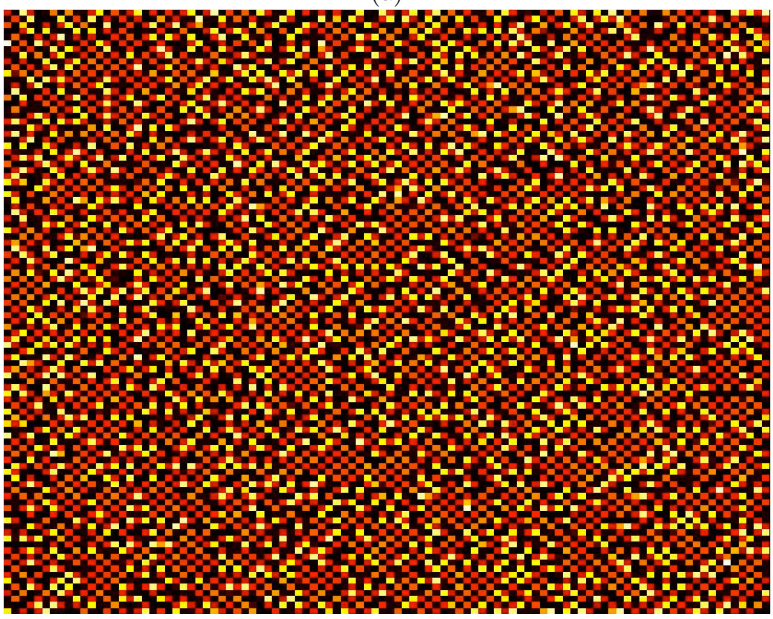

(b)

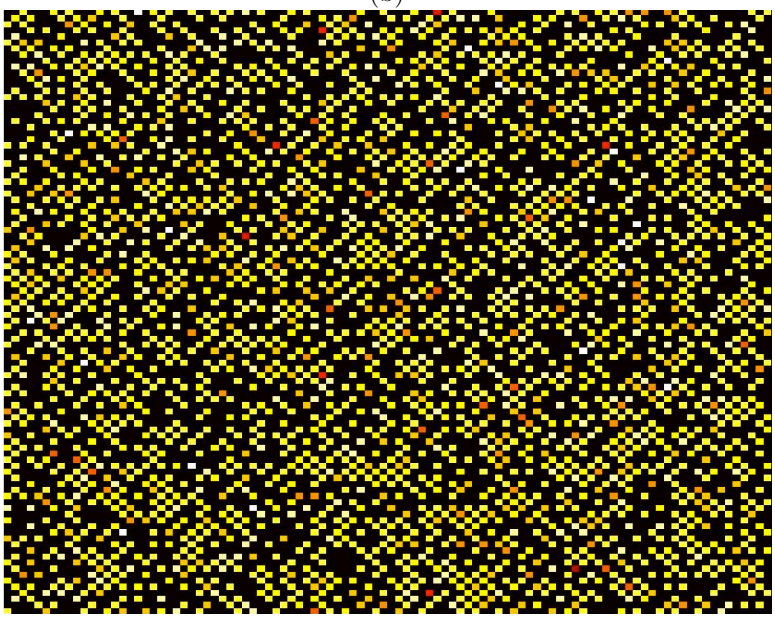

Figure 2.9: The vibrational population of the surface for a single trajectory at the conclusion of a CLIO FEL pulse (figure (a), 8 μs excitation) and 1 ms thereafter (figure (b), $k_{abs,CLIO} = 5$ x$10^7 s^{-1}$ for 8 μs excitation for both). For (a), the legend is: n=0-black, 10-red, 20-orange, 25-yellow, 32-white, highest level. For (b) : n=0-black, 5-red, 10-yellow, 12-white, highest level.

Chapter 3

Vibrational Pools at Solid-Diatom Interfaces: Chemical Potential and Emergent Correlation

3.1 Introduction

In an earlier chapter, we treated a diatomic adsorbate on a solid in terms of a distribution function at any time t, $P_n(t)$, corresponding to an equilibration among pools of N vibrational quanta in the adsorbate in various states n. The upper limit of $n \leq n_{max}$ in the one-quantum assisted exchanges was determined by the constraint of the Debye frequency ω_D of the solid.

Our prior theory treats the case where the domain is restricted.[1] This is expected to be the case at moderate intensities: high enough that pooling is faster than relaxation, but not high enough that $n > n_{max}$ can form. Whereas the rate for the 1 + 9 to 0 +10 pooling reaction was 5 x 10^7 s^{-1}, given that a 1 is adjacent to a 9, the rate of the 1+ 18 to 0 + 19 pooling reaction is 2 x 10^5 s^{-1}, given that a 1 is next to an 18. From prior rate constant calculations $\kappa_{19}/19$=1 x 10^4 s^{-1}. Thus, one may expect two-phonon pooling (e.g. 1+18 to 0 + 19) to be fast on this surface relative to relaxation when $P_1 > 0.05$, and it is not surprising that the kinetic Monte Carlo exceeds the one-phonon assisted limitation. Additionally, one expects quanta from higher pools to be mostly relaxed by the ms timescale.

3.2 Formation of higher pools

The mechanism of forming the higher pools, $n > 10$, under high intensity lasing is complex. The $n = 1$ initially form linearly, saturating quickly under FEL lasing and the $n = 2$ pools form as a result of 1+1 pooling among existing pairs, and forming at rate $W_{1,1}P_1$, as can be seen in Fig. 3.1. This result follows naturally from our prior discussion of second-order rate constants.[3]

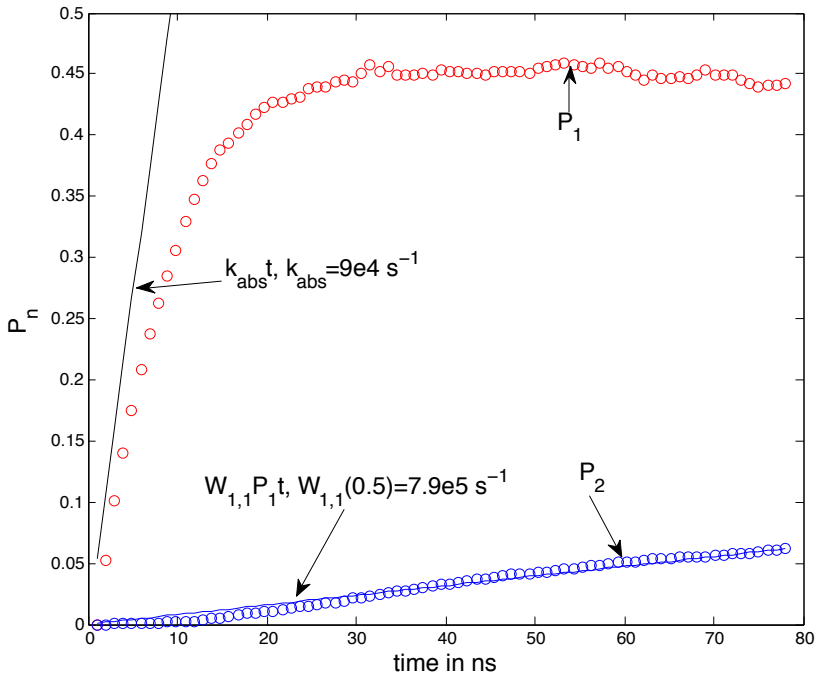

Figure 3.1: This figure shows the formation of P_2, noting $P_{1,ss} \approx 0.5$

Additionally, we find that the $n = 10$ and $n = 27$ pools form linearly with time. Beyond this, we observe no polynomial temporal pattern in the P_n buildup during lasing. This is consistent with the description of these states as bottlenecks, as assumed for the $n = 10$ state in prior work.[1]

To understand pooling in more detail, we consider the allowed P_n distributions and γ in the following section, before deriving the chemical potential for the CO:NaCl(100) surface specifically.

3.3 Evaluation of P_n for several N and γ

While the form of the distribution function in our prior work may be familiar to some from an earlier derivation in the gas phase,[13] we take the time now to review the general forms of P_n that can be taken for various levels of N. We note that, by the definition of N, γ satisfied the relationship:

$$\frac{N}{M} = \frac{\sum n e^{\gamma n - \frac{\epsilon_n}{kT}}}{\sum e^{\gamma n - \frac{\epsilon_n}{kT}}} \tag{3.1}$$

We have noted previously that this was the distribution function resulting from restriction of the surface to a constant number of vibrational quanta.[1] Varying γ and finding N from Eq. 3.1 we can elucidate this relationship, as in Fig. 3.2, choosing the appropriate γ for the amount of vibrational excitation. However, because small errors in this fit lead to exponential differences in P_n, the overall

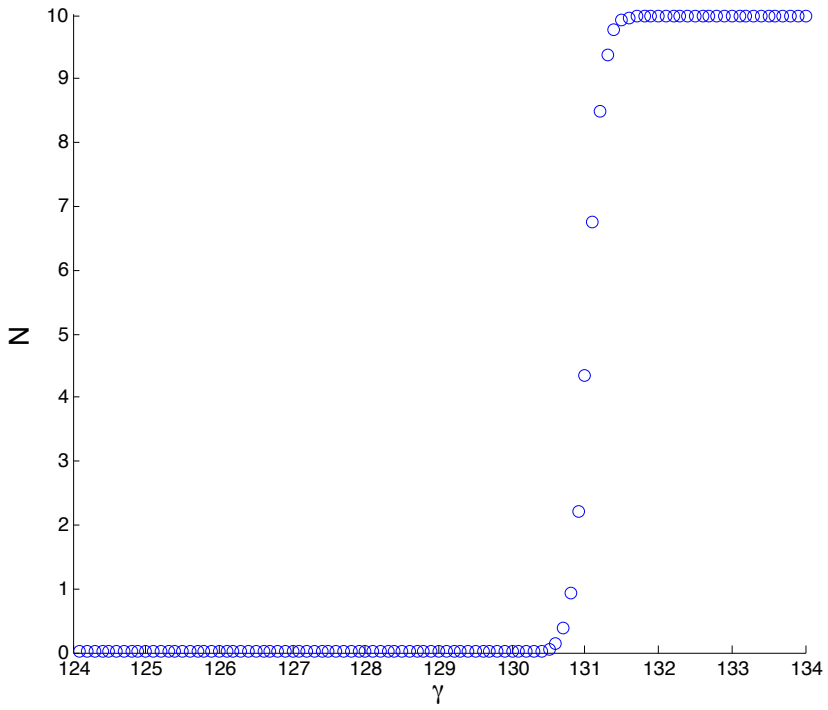

Figure 3.2: This figure shows N vs. γ for the domain restricted theory.

fit to observed P_n may not be very good even when the deviation from the linear fit relative to Boltzmann expectation, as in Fig. 1.1, is very small.

Other forms of the one-phonon restricted distribution function are possible, if other long-lived N (and thus γ) are observed experimentally. If $\gamma = 130$ we have the inversion as before, as seen in Fig. 3.3.

$\gamma = 125$ and 140 are evaluated for P_n and compared with the Boltzmann distribution in Figs. 3.4 and 3.5. Complete inversion, as in $\gamma = 140$ is unlikely with laser-initiated transfer, because of stimulated emission. When $\gamma = 125$, $n > 2$ populations are too small to amount to anything at 22K ($\approx 10^{14}$ sites within the laser spot). We mean only to stress that, in situations where there is not relative vibrational inversion on the n domain, there still may be deviation from the Boltzmann expectation.

3.4 Analysis of the Correlation Function vs. Distance of Separation

The appearance of a checkerboard in earlier heat maps on the CO:NaCl(100) monolayer surface was indicative of a nearest-neighbor anti-correlation between pools, as we have previously noted.[3]

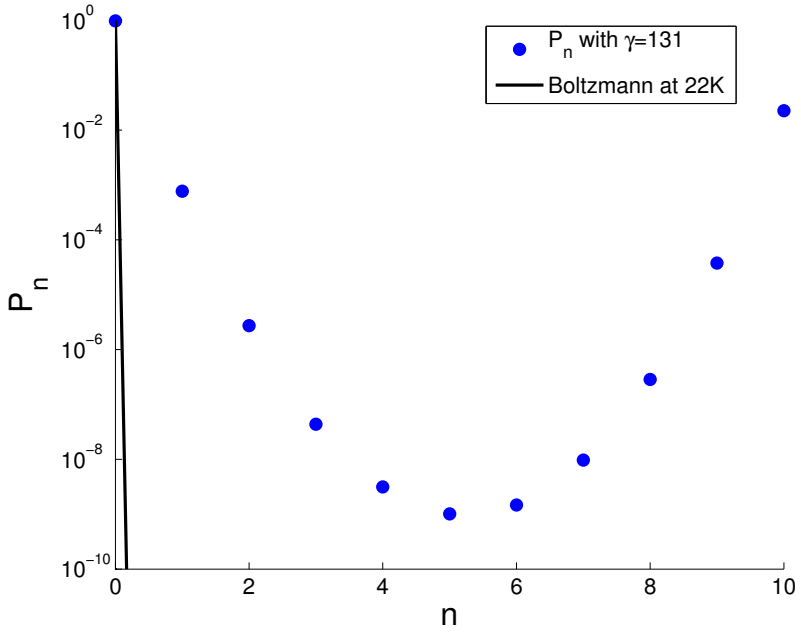

Figure 3.3: This figure shows the P_n compared to the Boltzmann distribution at 22K for $\gamma = 130$.

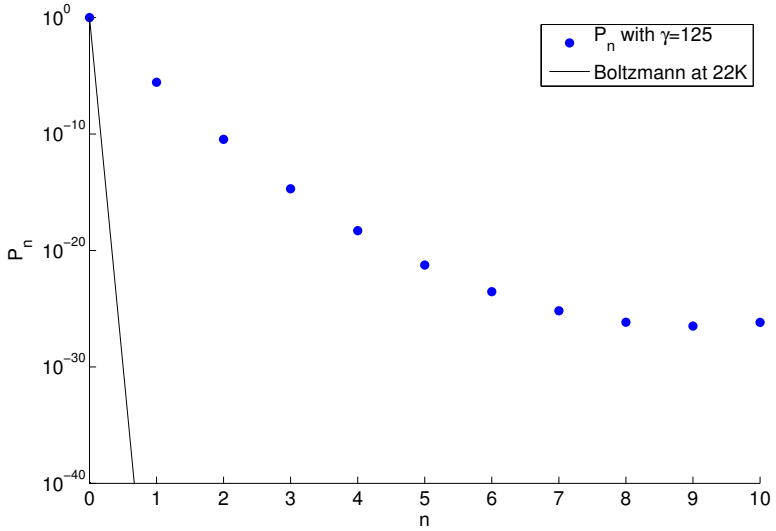

Figure 3.4: This figure shows the P_n compared to the Boltzmann distribution at 22K for $\gamma = 125$.

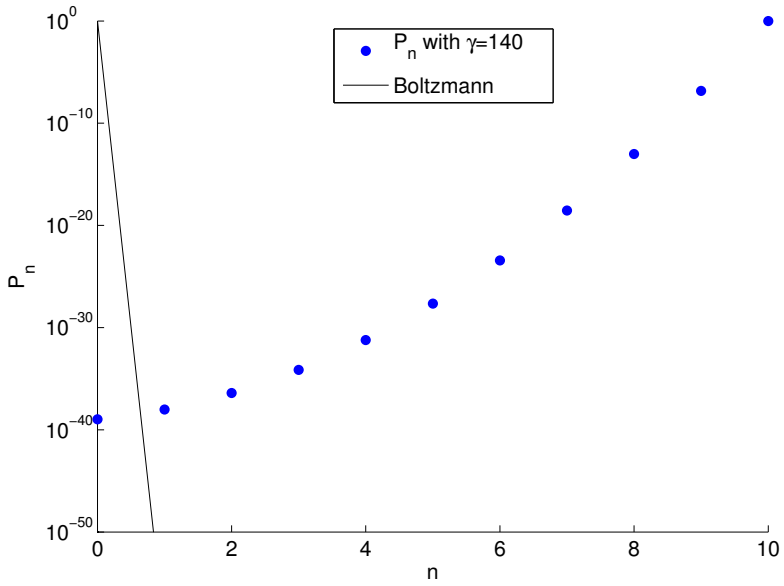

Figure 3.5: This figure shows the P_n compared to the Boltzmann distribution at 22K for $\gamma = 140$.

To examine whether this correlation extends further than nearest neighbor, we have calculated the pairwise probability of neighbors of every distance on a 100x100 surface from a previous experiment. Pairwise Probabilities of pools and pools ($P_{10,10}$) and pools and vacancies ($P_{10,0}$) vs. distance for the two conditions is measured in Fig. 1. Because of the residual checkerboard effect, pools are slightly anti correlated with the vacancies of the next two neighbors, with still 10% anticorrelation as far as 10 Angstroms from the pool (2.5 times the nearest neighbor distance of 3.96 Angstroms), 1ms following excitation by a free electron laser. At wide separations, the mean-field expectation for $P_{n,m}$ is recovered.

While this is only a two-dimensional calculation, presented in this chapter for the first time, it may have implications for the behavior of the vibrational populations at surfaces in conditions where relaxation is slow and the temperature is low, mean-field theory is not expected to hold for the vibrational evolution master equation, such as for multilayers of CO on NaCl(100).[12;11]

3.5 Introduction of the Free Energy and Chemical Potential

We treat the equilibrated system at long times, consisting of the pool of $n = 10, 9, 8$ with an upper cut-off at $n = 10$, and consisting of another phase, this the pool centered at a higher n, with no cutoff because of an alternative formation mechanism (e.g. under FEL lasing, as calculated before by kinetic Monte Carlo).[3] We proceed as we did previously,[1] and minimize total free energy subject to a given number of quanta. The result is the same as that obtained before, but now with no

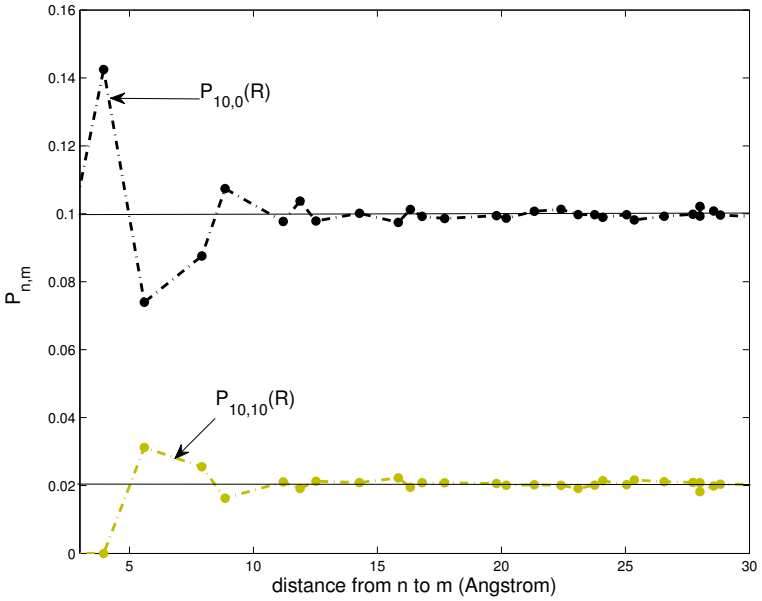

Figure 3.6: The vibrational pairwise population 1 ms following the beginning of lasing, compared with the mean-field expectation of the pair considered, the dashed lines are guides for the eye: (black)- $P_{10,0}$, the pairwise probability of a $n = 10$ state next to a $n = 0$ state (orange)-$P_{10,10}$, the pairwise probability of a $n = 10$ state next to a $n = 10$ state (note complete anti-correlation of nearest neighbors). The mean field result for $P_{10,0}$ and $P_{10,10}$ are given by the horizontal lines. Note that, for neighbors, mean-field is a bad approximation, but for $R >> R_0$, the nearest neighbor distance of 3.96 Angstroms, mean-field is recovered.

Debye-based constant constraining the pool to a restricted n domain. We have all pools using equilibration.

When only $n \leq n_{max}$ pool is present, namely at lower fluences, the sum over n was only up to $n = n_{max}$. We then have the free energy, F of a site, given that it is in a pool, given the P_n:

$$F = \sum_{n>0} E_n P_n + kT \sum_{n>0} P_n ln P_n \tag{3.2}$$

where

$$P_n(t) = \frac{e^{\gamma(t)n - \frac{\epsilon_n}{kT}}}{\sum_n e^{\gamma(t)n - \frac{\epsilon_n}{kT}}} \tag{3.3}$$

and we have avoided counting n=0 states because they are vacancies, not pooled vibrational quanta. Thus, for the free energy of the pool given only N:

$$F = \gamma N kT - kT ln(\sum_{n>0} e^{\gamma(t)n - \frac{\epsilon_n}{kT}}) \tag{3.4}$$

The remainder of this Chapter will focus on the confirmation of the derived form chemical potential of the first vibrational pool of monolayer ^{13}CO:NaCl(100), $0 < n \leq 10$, as given in Eq. 3.4, at both high and low fluence lasing conditions and short and long times.

3.6 Results and Discussion

We are interested in finding the chemical potential of the new pooled surface. We then define the chemical potential of the pool by a partial derivative with respect to the average number, and obtain $\mu_{pool} = \partial F / \partial N = \gamma kT$.

If one plots the free energy and average number, with each a function of the underlying time, as in Fig. 3.7 for an 8 ms CLIO trajectory, we find μ_{pool}=2120 cm^{-1}. This is approximately γkT, which was our prior domain-restricted fit under monolayer excitation conditions with 10^{-3} times the fluence of the CLIO.[1;3]

We establish the $N\gamma kT$ behavior of the free energy further with several examples from our prior work. For the monolayer, the results can be seen in Fig. 3.8 and for the 10^3 higher fluence condition from the FEL source, the results are given in Fig. 3.9.

These figures confirm the fit of the derived form of the chemical potential derived in Eq. 3.4.

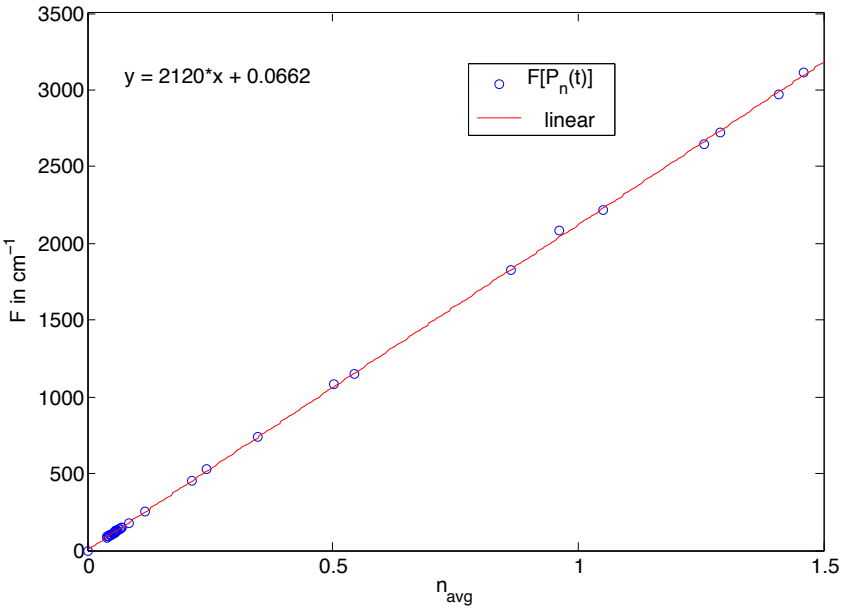

Figure 3.7: In this figure, we see F vs. N, and see the chemical potential (slope) is 2120 cm^{-1}. From γkT in our prior work, we had estimated 1960 cm^{-1} based on γ from the domain restricted theory.

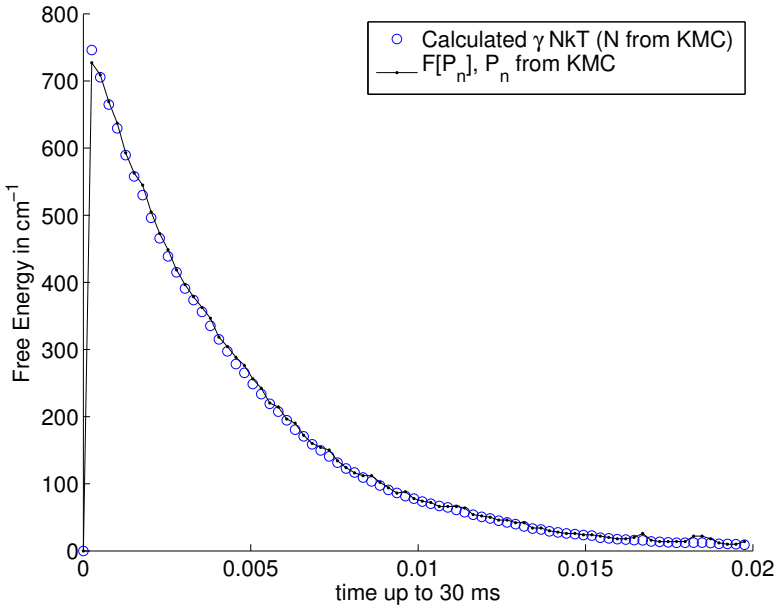

Figure 3.8: The fit of γNkT for 20 ms following Monolayer lasing.[2;1;3]

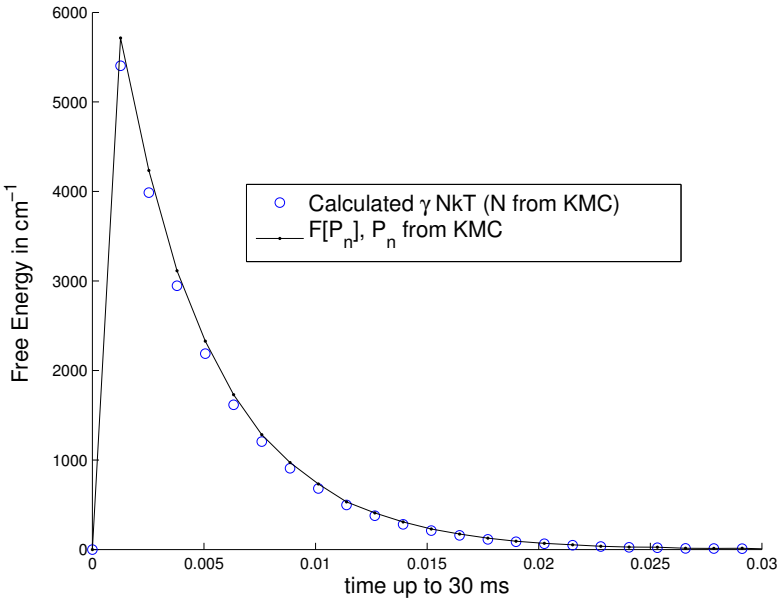

Figure 3.9: The fit of γNkT for 30 ms following CLIO lasing.[3]

3.7 Conclusions

We conclude that the behavior of vibrational pools under intense excitation to higher vibrational levels is usefully described by an addition to the previous theory: the description of pools in terms of free energy per pool of γkTN , or the chemical potential of a vibration in a pool ($\mu_i = \gamma kT$).

Chapter 4

On the Laser-Induced Desorption of H_2 from an H:Si(111) surface

4.1 Background and Introduction

Hydrogen surface chemistry has a rich history, and there was great interest in its behavior on semiconductor surfaces such as silicon[30;31;18;32;33;34;35;36] in the 1990s. This body of work includes low-energy probes such as infrared (IR),[33;31;37;30] Raman,[34;38] sum frequency generation (SFG),[4] thermal desorption,[39;40] and theoretical calculations of the H:Si(111) surface.[18]

At that time, single exponential recovery of the ground state with time constant 0.9 ns was observed.[4] This single exponential behavior has been taken by the authors as evidence against vibrational pooling on that timescale.[4] We have shown previously[1] that if pooling is the fastest rate, one expects single exponential decay of every state with the same decay constant as the recovery of the fundamental.

These SiH experiments[4;33;31;37;30;34;38;39;40] have previously been interpreted in terms of non-radiative (nr) deactivation by a multi-phonon excitation of the solid or possibly coupling to a bend.[31] There are two additional known non-radiative processes that can also cause vibrational exchange and are relevant for the present model: resonant vibrational exchange with nearby sites and non-resonant vibrational energy transfer (pooling and depooling).[9;10] These vibrational exchange mechanisms can in principle occur with sites further than nearest-neighbors, but we restrict the discussion to nearest-neighbors for simplicity.

Ma et. al.[19] have studied the theory of resonant exchange and non-resonant vibrational pooling and depooling in their three-state ($n = 0, 1, 2$) treatment of multiphoton absorption for this surface. They concluded that "if the lifetime of the excited state is long enough, the oscillator has the possibility to reach highly excited states through a series of pooling" steps. Previously, fluorescence of highly excited CO on NaCl(100) arising from the excitation of the CO fundamental by an infrared laser has been observed experimentally by Richardson and Ewing[41] and has been interpreted by Tully

and Corcelli in terms of vibrational pooling on that surface.[9;10] Our earlier work[1;3] confirmed and extended their model for CO:NaCl(100).

Depending on the incident light intensity, one might expect this effect to be observed for the H:Si surfaces as well, given the large mismatch between the Debye frequency of the solid (448 cm^{-1})[10] and the fundamental SiH vibration (2087.3 cm^{-1}) that requires many solid-state phonons to be excited at once, leading to the qualitative expectation of a slow relaxation rate of the SiH state with this mechanism.

In an earlier study,[20] results were given to show that it is possible to desorb molecular Hydrogen (a process that overcomes a bond of about 2.4 eV) using Free Electron Laser pulses in the infrared (at 0.26 eV) with power 1 kW/macropulse at room temperature.[20] It has since been indicated in later work that the authors no longer had access to a FEL needed to repeat the experiment under the same conditions. The original paper[20] has since been corrected, effectively retracted as not reproduced. However, they no longer had access to a FEL, and the present theory leads to results that are very sensitive to the intensity absorbed, so one may not expect the same results.

In the present chapter, we explicitly treat reactions between higher level vibrational states of SiH, building on a recent three-state model of H:Si(111) of Ma et. al.[19]. We use a Morse potential fixed to the first and second transitions of H:Si(111) to extrapolate rates of vibrational pooling and depooling following the method of Corcelli and Tully. Otherwise, we use the same models for relaxation and pooling as Ma et al. for ease of comparison.[19] We explicitly treat laser overlap with hot band states as well. This methodology extends the prior kinetic Monte Carlo work[9;10;1;3] to the H:Si(111) surface.

In order to compute the time-evolving vibrational probabilities for the states n on the surface, we use the same prescription as before for the calculation of the pooling rates as given in the Chapter Appendix. However, following previous experimental and theoretical work for this surface, we take the relaxation rate dependence on n to be:,[4;19]

$$\kappa_n = n\kappa_1 \tag{4.1}$$

with κ_1 the one free parameter in the model, the non-radiative decay rate of the n=1 state. While this parameter is free, in that it is not set by ab initio calculation, it will be fixed by the experimentally observed rate of decay,[4] as was the case on CO:NaCl(100).[1;3]

For H_2 desorption from the monolayer, the activation energy is 2.4 eV, or around 10 SiH vibrational quanta, as estimated by studies of thermally induced desorption.[42] This concentration of quanta in two nearest neighbors cannot be the case at low levels of excitation, because the cutoff suggested by the domain restricted theory is the supremum of $\omega_D/(2\omega_e\chi_e) = 448/90$, i.e. 5.[1] Because previous studies[3] and the previous Chapter observed anti correlation between pools and excitation

in neighbors, one needs pooling beyond n_{max} for two neighbors to reach the desorption threshold.

This requirement suggests the use of a Free Electron Laser, which provides, on average, frequent high fluence stimulation for 6-8 μs in $\approx 10^4$ micropulses, each some ps long and separated by fractions of a nanosecond. It was stated in the retraction of the previous experiment,[20] that the Vanderbilt Free Electron Laser is a unique light source for this experiment.[20] We note in passing that the Free Electron Laser at the Centre Laser Infrarouge d'Orsay (CLIO) facility has an almost identical power and pulse structure to that of the now defunct Vanderbilt source,[25] and suits the selective desorption experiment quite well. Our calculations of the FEL pulse could equally well describe either laser.

We can develop the theory further for the loss of H_2 pressure experimentally.[20] Let us assume that the desorption of H_2 occurs with effective first order rate constant k' for some concentration of excited SiH vibrations ($[SiH]$). Allowing for a pump of rate constant k, we have the following first order equation for the change in p_{H_2}, the pressure of H_2 remaining in the chamber:

$$\frac{dp_{H_2}}{dt} = k'[SiH] - kp_{H_2} \tag{4.2}$$

assuming a steady-state, $k'[SiH] = kp_{H_2}$, and given the first order loss relation $-d[SiH]/dt = k'[SiH]$, we then have

$$-\frac{dp_{H_2}}{dt} = k'p_{H_2} \tag{4.3}$$

So that the apparent half-life of the yield in the chamber gives information on the reaction rate, k_{rxn}, for instance, if we take take $k_{rxn} \approx k'/(< P_5 >)^2$. For the calculated value of $P_5 \approx 10^{-2}$ during lasing as in Fig. 4.2, the average value of P_5 over the 1/30 s time interval between pulses is $< P_5 >= P_5$ x $6/33,333 = 2$ x 10^{-6}, assuming all states completely relax immediately when the laser is not on. For a measured value of $k' \approx ln(2)/0.5$ s^{-1}, this implies a reaction rate constant of $\approx$1 x 10^{12} s^{-1}.

4.2 Results

The first calculations in this chapter follow the evolution of the vibrational populations on the surface without allowing desorption, and fix the free parameter (the system-bath coupling, effectively setting κ_n, the rate of decay to phonons). In these studies, we are able to determine if neighbors ever reach higher levels of excitation, after first fixing all the parameters in our model with relaxation lifetimes derived from apparent SFG decay time constant for the system.[4] One can see the fit, done at 95K in Fig. 1.

With the relaxation constant κ_1 fixed, we can then examine whether the conditions for a reaction exist on the surface at any point under the SFG pump conditions 35 μJ in a 20 ps pulse. The time

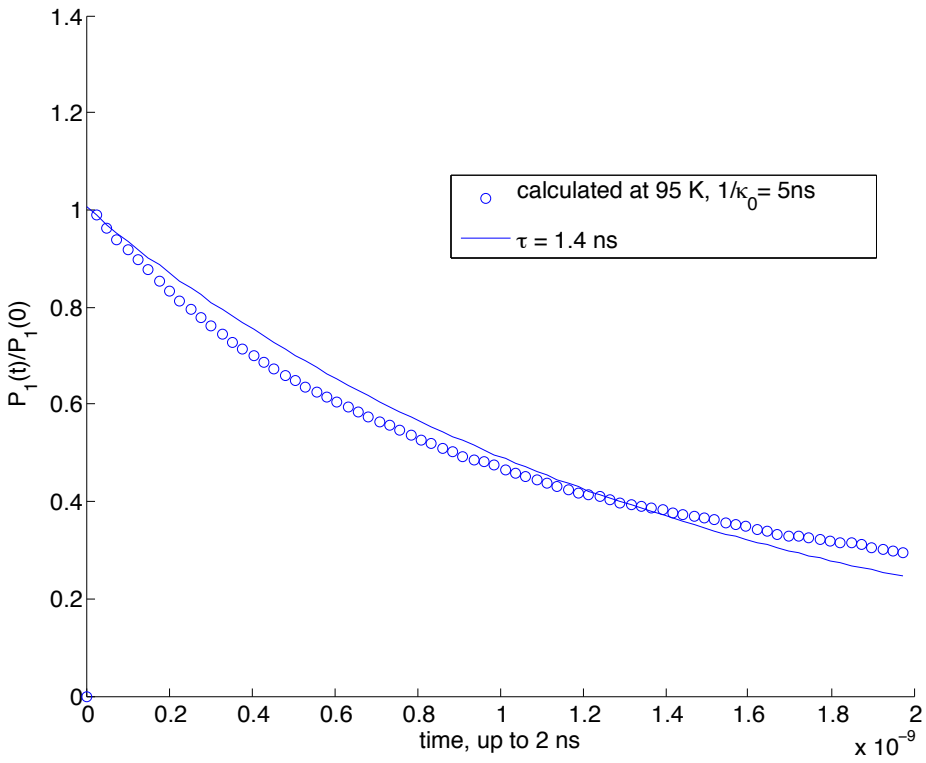

Figure 4.1: The fit to the experimental loss of P_1,[4] $\kappa_1 = 1/(5\text{x}10^{-9})$ s^{-1}

evolution of the vibrational populations is given in Fig. 4.2.

CLIO excitation (at 1kW/macropulse, $k_{abs} = (I\sigma)/(\hbar\omega) = 2$ x 10^9 s^{-1}) leads to some neighbors having combined vibrational energy of 10 quanta or greater (greater than the 2.4 eV activation energy). To examine desorption explicitly, we then extend the method to include an explicit description of the process of associative desorption in the Monte Carlo algorithm; A four frame visual overview of the evolution of the H_2 molecules evolving from the lattice is given in Fig. 4.3 (a)-(d). For now, in the calculations, we assume that the rate constant for associative desorption is around 1 x 10^{12} s^{-1}, consistent with our estimate from the end of the first section in this chapter (1 x 10^{12} s^{-1}) and the order of magnitude of the fastest rates considered (resonant vibrational transfer), and simply add this rate process in with all the others (pooling, depooling, and relaxation to phonons). The actual rate of reaction may be faster: this reaction rate constant is 1/16 the first-order pre-factor from thermal desorption calculations (6 x 10^{13} s^{-1}).[40]

We also investigate the evolution of the desorption yield against fluence variation computationally, now without any free parameters, to lay the groundwork for the proposed experiment. One can see the dependence of the desorption yield of H_2 on fluence in Fig. 4.4.

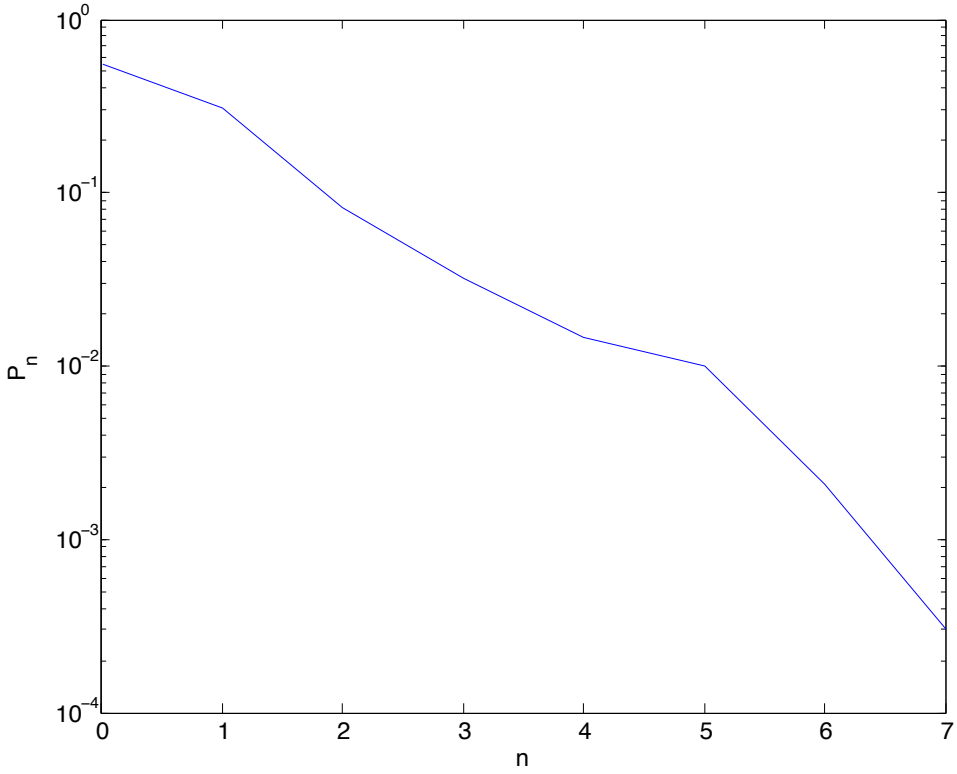

Figure 4.2: The P_n vs. n 1.9 ns after lasing with prior conditions.[4]

4.3 Discussion

At short times, for instance in the 2 ns following the 20 ps pulse of the prior SFG pump,[4;16] it is impossible for any pair to have $n = 10$ or greater, because of the anticorrelation of pools,[3]. Consistent pulsed excitation, pooling, and relaxation are required to reach a combined $n = 10$.

We note that the saturation behavior of pooling with intensity is at odds with the quadratic behavior described in previously retracted experimental results,[20] providing the present chapter with further motivation in determining the H_2 dependence on light Intensity.

Previous calculations including both inelastic phonon scattering and phonon emission assisted vibrational pooling indicate that pooling by phonon emission may be expected to dominate when the temperature is low.[19] Thus, given the three temperatures we could choose to fix the final parameter of our model, T = 95, 300 and 460 K from the prior SFG lifetime experiment,[4] we choose the lowest temperature, T=95K, and draw conclusions about desorption only at this low temperature. Since the prior FEL was performed at room temperature, the comparison is indirect, and could be improved at room temperature by the inclusion of inelastic phonon scattering rate constants.

In an analysis in our previous work,[1] from previous calculations of the pooling rate constant,[19] the rate constant for the 1 + 1 to 0 + 2 pooling reaction can be as high as $\approx$ 2 x 10^8 s^{-1} on H:Si(111) under some experimental conditions.[4;16] Based on the trends in pooling rate constants

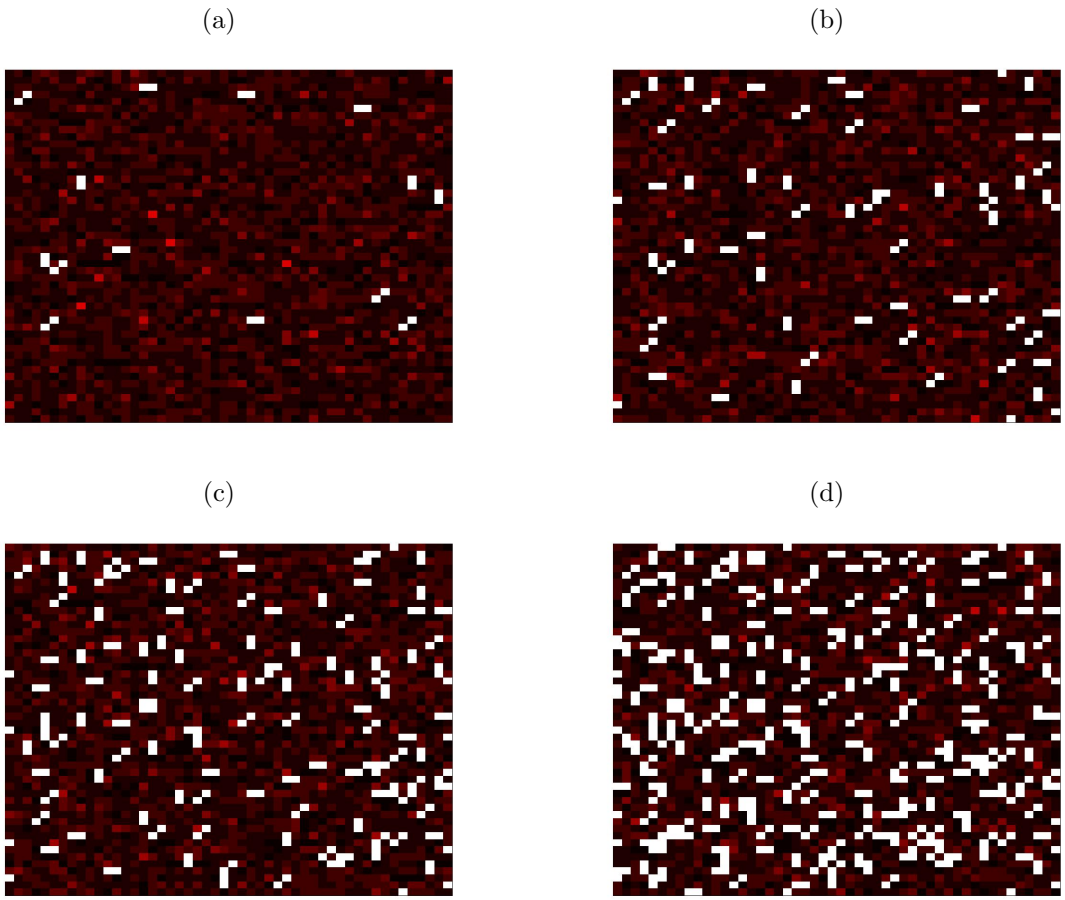

Figure 4.3: Snapshots of the evolution of H_2 from a 50x50 surface under FEL excitation: (a) after 100 ns (b)after 500 ns (c) after 1μs (d) halfway through lasing. We note that the colors indicate black for $n = 0$ white for $n = 21$ in (b)-(d), with $n = 21$, outside the $n = 1-20$ domain, used to mark the sites that have evolved off the surface by associative desorption (white). While we are unable to render the 111 surface (a hexagonal lattice), the square lattice connectivity in figures shown includes diagonals up and to the right and down and to the left of each site, effectively giving 6 neighbors of equal distance. Thus we see diagonally desorbed molecules on the square lattice representation of the 111 surface.

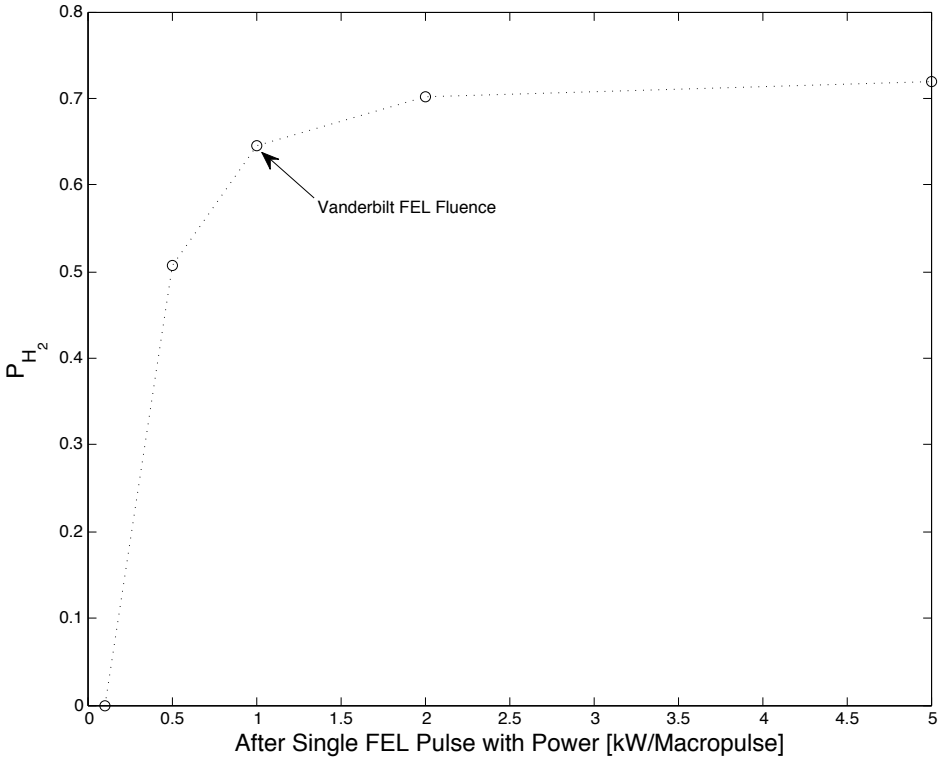

Figure 4.4: Yield of H_2 after a single macropulse vs. Power of macropulse, assuming fast-pooling (calculations shown for $\mu' = 1e$).

for CO:NaCl(100),[1] we expect the pooling rate constant for the $1 + n_{max} - 1$ to $0 + n_{max}$ pooling reaction, k_{pool}^{SiH}, to be 7 x 10^9 s^{-1}. In this case, the calculated pooling rate constant is $\approx$ 10 times the observed rate of loss of single quanta to the solid (λ^{SiH} $\approx$1/0.9 ns =1 x 10^9 s^{-1}), and $P_1 >> 0.1$ would meet the equilibration condition given in Chapter 1 as $k_{1,9}^{pool} P_1 > \lambda$. However, we note that the pooling rate constant leading to fast-pooling requires the incorporation of inelastic scattering by phonons.[19]

As a first approximation, we take the transition dipole moment derivative from the previously reported cross-section,[43] finding a transition dipole of μ'_{exp} =0.45 e, $\sqrt{5}$ larger than that derived from the derivative of the previous Density Funcional Theory calculations of the dipole moment, 0.2 e.[19]

The change of transition dipole from the prior calculation[19] leads to an increase in the rate constant by phonon emission from the previously calculated[19] $k_{1,1}^{pool}$ = 4.2 x 10^6 to 6.2 x 10^7 s^{-1}, and $k_{1,4}^{pool}$ = 5 x 10^8 s^{-1}. By the estimate developed in our prior work,[1] this is a regime that is not fast-pooling equilibrated, because $k_{1,4}^{pool} P_1 < \lambda$ =1 x 10^9 s^{-1} for all P_1. For the moment, since the transition rate constant goes with the 4^{th} power of transition dipole (see Chapter 2 Appendix A), we can modify this equation for unknown dipole moment to be $\mu' = \alpha \mu'_{exp}$, allowing μ' to vary from the experimental value. The fast pooling test then becomes (5 x 10^8)$P_1 \alpha^4 < \lambda$ =1 x 10^9 s^{-1}, which can be realized for $\alpha > (4)^{1/4} = 1.414$ (assuming $P_1 \leq 0.5$). Especially given the recent retraction by the same lab as the cross-section experiment, presented as a personal communication in the literature,[43] it would be preferable to have the IR absorption cross-section for the H:Si(111) stretch determined in the literature independently. Regardless, we calculate the kinetic Monte Carlo for the surface to see if desorption occurs by pooling including only phonon-emission, even outside the fast-pooling regime.

One can also examine the spectrally integrated SFG intensity in the previous hot band pump-probe experiment for evidence of pooling on H:Si(111).[16] We calculate that, after pumping, the spectrally integrated SFG intensity is approximately 1/3 the value before pumping (inferred from Fig. 1 of the reference[16]). A possible interpretation for this reduction in the spectrally integrated signal is that pooling is fast, and much of the excited population is at the pooling maximum (n_{max}=5 for H:Si(111)). In the previous experiment,[16] following the pump, the SFG probed the 1840-2125 cm^{-1} range.[16] If one extended the SFG probe range to 1600-2125 cm^{-1} following the same pump as before,[16] then it may be possible to see if the majority of the spectrally integrated SFG intensity after pumping occurs at $n = 5$. If fast-pooling occurs, one expects to see the $5 \rightarrow 6$ transition dominate the post-pumping SFG, which is expected to be around 1630 cm^{-1}.

Additionally, as in Figs. 4.3 (d) and 4.4, we note that the yield approaches an anti-percolation threshold at high fluences. The physical maximum for number of sites desorbed is $1 - 1/(n_{neigh} + 1)$ where n_{neigh} is the number of neighbors for each site, because each site must have a neighbor

still on the surface with whom to react. This could explain one difference between Temperature Programmed Desorption (TPD) and Laser Induced Thermal Desorption (LITD) for the H:Si(111) surface: LITD apparently leaves ≈ 0.1 of the surface unreacted, compared with TPD.[42] Such a fractionally covered surface is measurable by either Atomic Force Microscopy or Second Harmonic Generation[44] following desorption.

4.4 Conclusions

In conclusion, in this chapter we present several results for H_2 desorption from the H:Si(111) surface that prompt the proposed re-evaluation experimentally and further research on the mixed isotope surface. Despite not reaching the regime of fast-pooling for transfer by phonon-emission only, we nonetheless recover the possibility of desorption without any free parameters in the kinetic Monte Carlo. We note the following results, which may be tested experimentally:

1- The desorption of H_2 from H:Si(111) is expected following excitation by a sufficiently intense Free Electron Laser.

2- Saturation dependence of H_2 yield with intensity per macropulse, as in Fig. 4.4, is observed, as opposed to the I^2 dependence reported in the retracted experimental reference.[20]

3- The final surface is expected to reach an anti-percolation threshold: not all Hydrogen will evolve off the surface by associative desorption, leaving a minimum of 14% for H:Si(111), and $1/(n_{neigh}+1)$ more generally for a vibration with n_{neigh} neighbors.

Chapter 5

Self-shielding in the $E^1\Pi(1)$-$X^1\Sigma_g^+(0)$ band of CO in a hot solar nebula

5.1 Introduction and Background

Calcium-Aluminum-rich Inclusions (CAIs) are some of the oldest condensates in our solar system, estimated to be about 4.6 billion years old.[45] Since their discovery,[46] however, scientists have been puzzled by the near unity slope of their three-isotope enrichment plot. Suffice it to say that the observed effect in these plots is the enrichment of the rarer O isotopes (^{17}O and ^{18}O) with respect to the original isotope when compared with levels elsewhere. A recent proposal put forth by Clayton,[47] who made the initial discovery of the isotope effect in CAI's in 1973, suggests carbon monoxide self-shielding at the X-point (hereafter X-pt.), may be responsible for this effect. A substantial portion of the astrophysics community,[48;49] however, doubts this is a viable mechanism due to the high temperatures (1000-1500 K) in the early solar system at this location, among other concerns. Determining the validity of this model was a project for several of the first years of study, with a longer term goal of elucidating the mechanism for oxygen isotope effects in CAIs, a problem that has now gone unsolved for 35 years.

Let us take a moment to examine Claytons hypothesis further. The absorption lines to the same electronic states of CO and its isotopomers are at slightly different frequencies due to the different masses of Oxygen isotopes. As $C^{16}O$ is much more abundant than $C^{17}O$ and $C^{18}O$ (2600:1 and 500:1 abundances respectively) regular CO will quench its frequency of light closer to the light source than these isotopomers. As such, more of the rare isotopic CO is cleaved, on average, further from the light source than the regular isotopomer, leading to a spatial separation of isotopes. If CAIs then formed in a region of heavy atom isotopic excess, this could be an explanation for their observed unusual isotopic distribution. Claytons proposal is that this spatial separation left a region

of isotopically enriched CO around 0.035 AU from the proto-sun at a temperature of between 1000 and 1500 K.

The predissociative state attained by a band 31 transition ($X^1\Sigma_g^+(0)$ to $E^1\Pi(1)$) is responsible for 58% of $C^{18}O$ photodissociation in a translucent cloud model,[50;51] and accounts for between 36 and 63% in other isotopomers (^{13}CO and $^{13}C^{18}O$). It dominates the dissociation and preferential dissociation leads to isotope effects, and it lies between 91-110 nm, a region that has little H_2 absorption at low temperatures. As such, it is the natural starting point to test Claytons hypothesis, and our calculations below take it as the only source of C^XO isotopomer fractionation. We assume throughout that the dissociation effects of $^{13}C^XO$ on oxygen isotope ratios is small compared to $^{12}C^XO$, since the $^{13}C^XO$ isotopomer accounts for only about 1% of the overall molecular abundance in the nebula.

Claytons hypothesis is not alone in the attempt to explain the mass-independent isotope effect in CAIs. Another such theory, proposed by Lyons and Young,[52] suggests CO self-shielding in a more distant (and thus colder) region of the solar nebula. A second such theory, proposed by Marcus,[53] involves isotope selective chemical reactions on the surface of CAI grains. This model assumes the isotopic composition of the sun is like that of the Earth, which is inconsistent with more recent measurements.[54] Nonetheless, the proposed chemistry of that model remains a possibility.

A similar mass-independent isotope effect has been observed in ozone both in the lab[55] and in the upper atmosphere.[56;57;58;59;60] Initially a self-shielding of O_2 mechanism was proposed,[50;51] but that was quickly shown to be unlikely.[61] Recent work[62] indicates that RRKM theory, with a non-RRKM symmetry-based modification, applied to the ozone formation reaction is sufficient to explain the observed isotope effect.

Here, we evaluate self-shielding at the X point, following Aikawa and Herbst,[63] the equations describing the temperature and number density of H2, in a minimum-mass solar nebula (MMSN) are the following:

$$T(R) = 28(\frac{R}{100})^{-0.5} \tag{5.1}$$

$$n(R) = n_0(\frac{R}{100})^{-}2.75exp(-d_0(\frac{1}{R} - \frac{1}{(R^2+Z^2)^{-}.5})) \tag{5.2}$$

where n_0 = 1.9 x 10^9 cm^{-3}, $d_0 = GM_{sun}\mu_{gas}/(kT)$, and R is the distance from the Sun in units of AU (1 AU = 1.5 x 10^{13} cm) along the midplane. Also, G = 6.67 x 10^{-8} dyne/cm^2/g^2 , M_{sun} = 2 x 10^{33} grams, and μ_{gas} = 2.4 x mass of a H atom. Gas pressure is obtained from P = nkT. Note that d0 is a function of R, as temperature also depends on R. Z is the height above the midplane of the nebula, also in units of AU (see figure 1 for clarification). Our calculations are performed at the

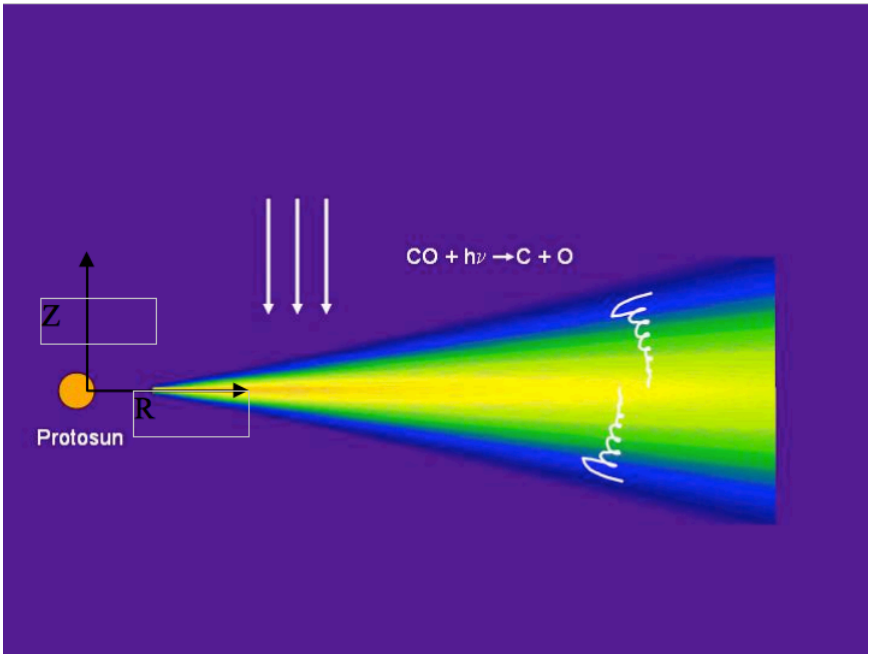

Figure 5.1: A visual representation of the Aikawa-Herbst model. The colors indicate the number densities of molecular hydrogen (red-highest, yellow-medium high, green-medium low, blue- lowest). The arrows in the negative z-direction indicate the direction of incident intensity. The spirals at large R are representative of vertical mixing. Their amplitude indicates the strength of the mixing. Reproduced with permission.[5]

X-point (R=0.035 AU, Z=0), which results in high densities of all gases.

To better understand the model, consider Fig. 5.1. The region Clayton shielding will take place is at the origin of the colored region. The origin is referred to as the X-pt. because the predominant wind in this protonebular model is outward along the edges of the disk, and the X-pt. is then the place where the top and bottom winds of the disk meet. One can see that the X-pt. is a region of very high density, and, as discussed earlier, very high temperature. In our model, the predominant light intensity comes from the Z direction i.e. from starts other than the sun. That area of low density where the incident intensity originates is called the Inter-Stellar Medium or ISM. To modify this near the X-pt. in our model, the intensity dependence is as if coming from the proto-star, but we still take the incident intensity coming from along the Z axis.

Note that, in our model, the angle of incidence of incoming light is along the Z direction, but with the intensity of the proto-sun. This makes our model different from Claytons (where incident light is along the R direction) when we calculate shielding effects in section III, and this approximation was made because the computational machinery already exists for this model.[52] As such, the present conclusions are for our pseudo-Clayton hypothesis, where the light is incident from the top of the nebula. Preliminary calculations for shielding with the correct geometry, incident light along the R-axis, indicate little change.[5]

Table 5.1: Molecular Constants for the various isotopomers of CO in the X^1S_g ground state. All values given in cm^{-1}. Note that e-parity is used for the P and R branches and f-parity is used for the Q branch.

X^1S_g	$^{12}C^{16}O$	$^{12}C^{17}O$	$^{12}C^{18}O$
B_0	1.92	1.87	1.83
D_0	6.1203 x 10^{-6}	5.814 x 10^{-6}	5.5300 x 10^{-6}
H_0	5.4794 x 10^{-12}	5.074 x 10^{-12}	4.733 x 10^{-12}

Table 5.2: Molecular Constants for the various isotopomers of CO in the E^1P excited state. All values given in cm^{-1}. Note that e-parity is used for the P and R branches and f-parity is used for the Q branch.

E_1	$^{12}C^{16}O$	$^{12}C^{17}O$	$^{12}C^{18}O$
v_1	95082.93	95056.02	95031.9
B_e	1.94	1.89	1.85
D_e	6.67 x 10^{-6}	6.0 x 10^{-6}	4.54 x 10^{-6}
B_f	1.93	1.88	1.84
D_f	6.64 x 10^{-6}	6.0 x 10^{-6}	5.13 x 10^{-6}

5.2 Computation of Absorption Spectra

The spectrum for the $X^1\Sigma_g^+(0)$ to $E^1\Pi(1)$ transition has been determined with the high precision of .003 cm^{-1} per resonance by Ubachs, et al.[64] The importance of the high resolution spectrum is that its correspondingly highly accurate molecular constants allow for reasonable extrapolation to high temperatures, such as those found near the X point. Given this high resolution spectrum and its correspondingly accurate molecular constants (see Tables 5.1 and 5.2), line positions in our synthetic absorption spectra were calculate dusing the formula:

$$E_E(J') - E_X(J'') = v_E + B_E J'(J'+1) - D_E(J'(J'+1))^2 - B_X J''(J''+1) + D_X(J''(J''+1))^2 \tag{5.3}$$

where J is the $X^1\Sigma_g^+(0)$ rotational state, J the $E^1\Pi(1)$ rotational state, B the rotational constant, and D the centrifugal distortion constant (given in Tables 5.1 and 5.2). We proceed to populate the vibrational and rotational levels of the $X^1\Sigma_g^+(0)$ state thermally, recording the Boltzmann population of each level. We consider the first 150 rotational levels (J) of the the ground vibrational state (v=0), and their corresponding 150 rotational levels for the excited state (J with v=1). The population of the $X^1\Sigma_g^+(0)$(v=0,J=150) state is 1.359 x 10^{-17} at 1500K, indicating further rotational levels need not be considered.

The computation of the absorption spectrum was carried out using a Voigt lineshape approximation for each line position (see Chapter Appendix for more detail). This approximation has shown to be valid in many regimes,[65] including the Gaussian and Lorentzian widths for which we use it here. We take the natural Lorentz linewidth of all CO isotopomers to be 0.034 cm-1 (found in Ubachs for

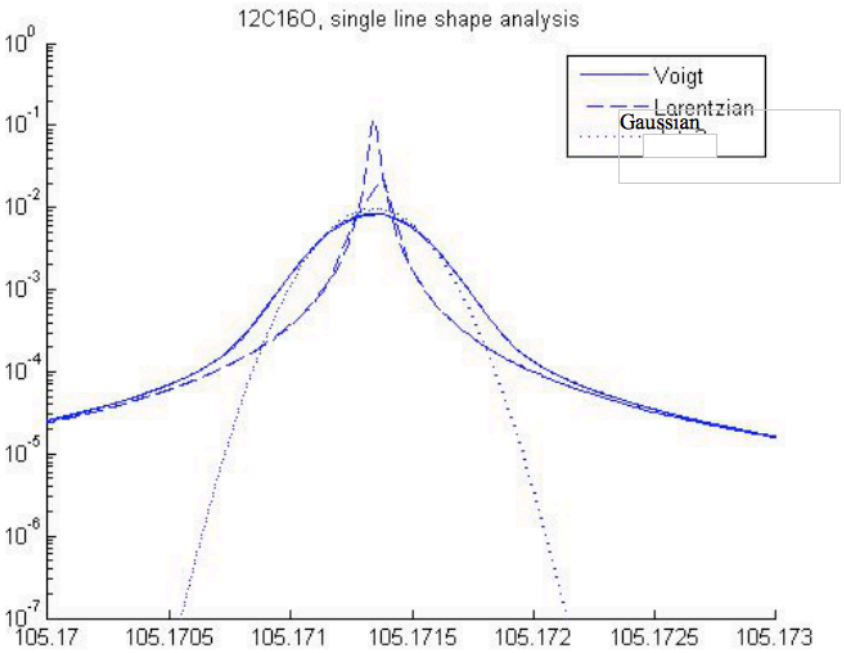

Figure 5.2: A comparison of the Voigt, Lorentzian, and Gaussian lineshape for a single transition.

$^{12}C^{16}O$)[64] and the Doppler width to have the usual temperature dependence (see Chapter Appendix for more details). The Voigt profile, $\Phi_{v'',J'',v',J'}$ is normalized so that $\int \Phi_{v'',J'',v',J'} dv = 1$. The Voigt profile has a Gaussian dependence near the center and a Lorentzian dependence in the line wings, which is evident in Figure 5.2.

The peak intensity for a given v, J, J band is determined using the following formula :

$$\sigma_{C^xO}(v, J'', J') = \sum_{J''} N(J'')\sigma_{v'',J'',v'J'} \tag{5.4}$$

for a particular isotopomer C^XO where $N(J'')$ is the normalized Boltzmann weight of that rotational level, i.e.

$$N(J'') = \frac{(2J''+1)e^{-\theta_r J''(J''+1)/T}}{q_{rot}} \tag{5.5}$$

where θ_r is the rotational temperature of C^xO (equivalent to B_0 for each isotopomer: 2.77 K, 2.70 K, and 2.64 K for $C^{16}O$, $C^{17}O$, and $C^{18}O$ respectively), J and T as defined previously, and q_{rot} the rotational partition function given by the 2^{nd} order expansion:[14]

$$q_{rot} = \frac{T}{2\theta_R}(1 + \frac{\theta_r}{3T} + \frac{1}{15}(\frac{\theta_r}{T})^2) \tag{5.6}$$

$\sigma_{v'',J'',v',J'}$is the cross-section for each rovibrational transition $(v'', J'' \rightarrow v', J')$, satisfying the fol-

Table 5.3: Comparison of $f_{v'',v'}$ for different isotopomers. All values from Eidelsberg.[8]

Isotopomer	Band 31
$^{12}C^{16}O$	2.4723 x 10^{-3}
$^{12}C^{18}O$	2.4697 x 10^{-3}
$^{13}C^{16}O$	2.4698 x 10^{-3}
$^{13}C^{18}O$	2.4671 x 10^{-3}

lowing relation:

$$\sigma_{v'',J'',v',J'}(\omega) = \frac{e^2\pi}{m_e c} f_{v'',J'',v',J'} \Phi(\omega) \tag{5.7}$$

where $\Phi(\omega)$ is the normalized Voigt profile and $f_{v'',J'',v',J'}$ is the absorption oscillator strength.

The absorption oscillator strength is obtained from the band oscillator strength $f_{v'',v'}$ using the formula:[8]

$$f_{v'',J'',v',J'} = f_{v'',v'}\left(\frac{\omega_{v'',J'',v',J'}}{\omega_0}\right)\left(\frac{S_{J''}}{2J''+1}\right) \tag{5.8}$$

Where the is the position of the transition, ω_0 is the band origin (the position of the fictitious transition v',J'=0→v",J"=0), S_J the Honl-London factor chosen appropriately for the band (P,Q, or R) and the band oscillator strength $f_{v'',v'}$ is obtained from Eidelsberg (2.4723 x 10^{-3} cm^2).[66] For the $X^1\Sigma_g^+(0)$ to $E^1\Pi(1)$ transition, the appropriate Honl-London factors are:[66] $S^R_{J''} = (J''+2)/4$, $S^Q_{J''} = (2J''+1)/4$, $S^P_{J''} = (J''-1)/4$. The total $\sigma_{CO}(\lambda)$ profile was obtained by adding all rotationally allowed transitions $\sigma_{CO}(\lambda, J'', J')$.

We have made the approximation that the band oscillator strength is constant in all isotopomers at 2.4723 x 10^{-3}. This is a good approximation in the band under consideration, see Table 5.3.

This analysis was performed for each of the transitions from the ground vibrational and the first two excited vibrational states of the $X^1\Sigma_g^+(0)$ to $E^1\Pi(1)$ transition (with Honl-London factors modified accordingly for each transition). The perturbation of this transition by the $k^3\Pi(6)$ state has been well characterized[64] as well. While this interaction will perturb the resulting synthetic spectrum and self-shielding calculations, as its rotational level dependence differs between isotopomers, we argue in the following section that its effect is negated by the shielding by H_2 in the nebula at such high temperatures. The same argument goes for the plethora of other, as yet uncharacterized, near-resonant excitations that will affect this transition at such high temperatures.

The calculation of a complete CO spectrum is constrained by the lack of highly accurate values for molecular constants of other electronic levels and other perturbative interactions. This accuracy is absolutely crucial at temperatures as high as 1500 K, as highly excited rotational levels are populated and small discrepancies in molecular constants or interactions begin to be magnified, resulting in incorrect line positions for the higher J transitions have increased cross-sections due to the thermal

population of the ground state.

The result of this calculation at 300 K can be compared to the experimental results of Stark et. al.[6] at 300 K for verification (Figs. 5.3 (a) and (b)). As we will be extrapolating our results to high temperatures, the low temperature verification must be very close to exact, which is borne out below. One substantial difference, the ratio of the Q/R branch is about 10:1 experimentally and about 5:1 in our simulation. However, because of instrumental saturation of the lines, their values are meant only as a lower bound to the peak absolute cross-section.[67] As such, the line cross-sections of the R branch may lie farther from the experimental lower bound than the Q values, resulting in the observed discrepancy. Additionally, the height of the Q-branch is more sensitive to the observed natural linewidth of the system, and a linewidth larger than the reported value of 0.034 cm^{-1} would manifest itself in a higher Q/R ratio, as well as a wider Q branch, both of which are observed.

Eidelsberg et. al.[8] report an observed temperature dependence of cross-section. Temperature dependence of peak intensity in our model arises from the Boltzmann distribution, as well as thermal broadening. The lineshapes are normalized (each band has same integrated intensity) so that a wider distribution means a slightly lower peak. Additionally, as one populates more rotational modes, each rovibrational transition carries less weight. The resulting temperature dependence of our spectra can be clearly seen in Fig. 5.5.

We then calculated the spectra for $^{12}C^{16}O$, $^{12}C^{17}O$, and $^{12}C^{18}O$ at 1500 K, the approximate temperature at the X point. These spectra are included below in Fig. 5.5 . The bandhead arising in the $^{12}C^{18}O$ spectrum is of particular interest (Fig. 5.6), as it has not been observed experimentally.

This bandhead is believed to be a feature of the high temperature $^{12}C^{18}O$ spectrum, as it arises directly from the molecular constants in Ubachs et al. From Herzberg[68] the transition frequency is given by:

$$\omega = \omega_e + (B_E + B_X)m + (B_E - B_X - D_E + D_X)m^2 - 2(D_E - D_X)m^3 - (D_E - D_X)m^4 \quad (5.9)$$

where m = -J (ground state) for a P-branch. Taking the derivative with respect to m yields Fig. 5.7. The zero of the graph corresponds to the rotational state of the bandhead. Thus the bandhead is a direct result of the spectroscopic constants, and is located between the 66th and 67th rotational state.

5.3 Line-by-line calculation of CO photodissociation

Given the spectra calculated above, we used an existing model to solve a one dimensional mass-conservation equation including chemical production and loss to determine the overall volume fraction of a given atom or molecule. This model, used in Lyons and Young,[52] allows for vertical mixing,

(a)

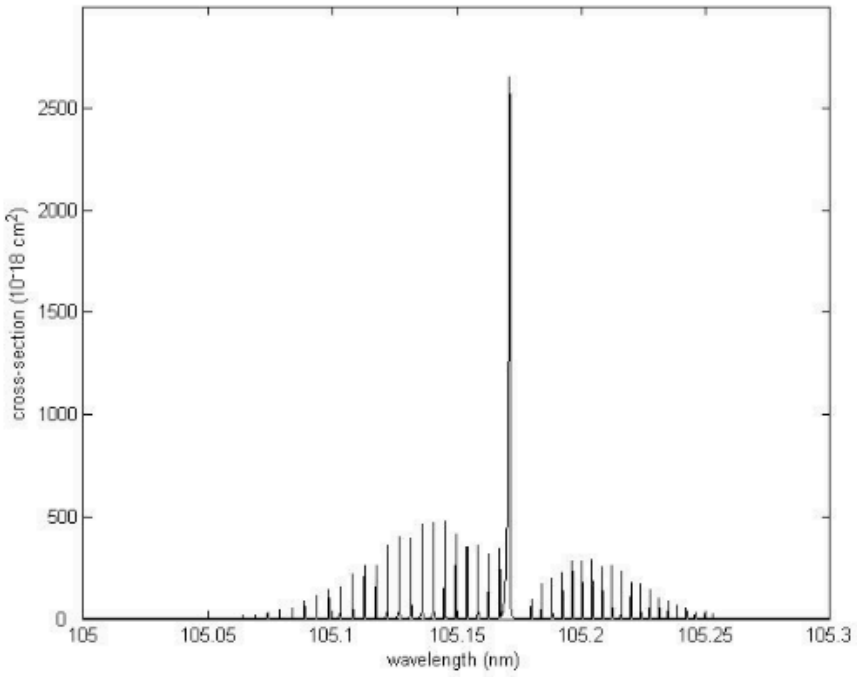

(b)

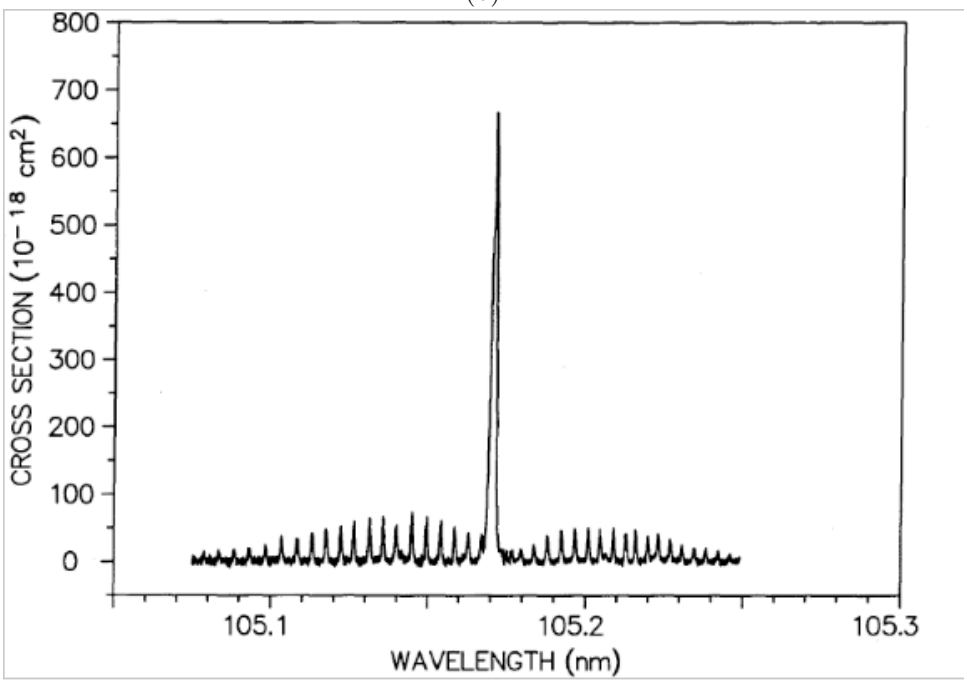

Figure 5.3: (a) The synthetic $^{12}C^{16}O$ spectrum calculated at 300K. (b) Reproduced from Stark et. al.[6]

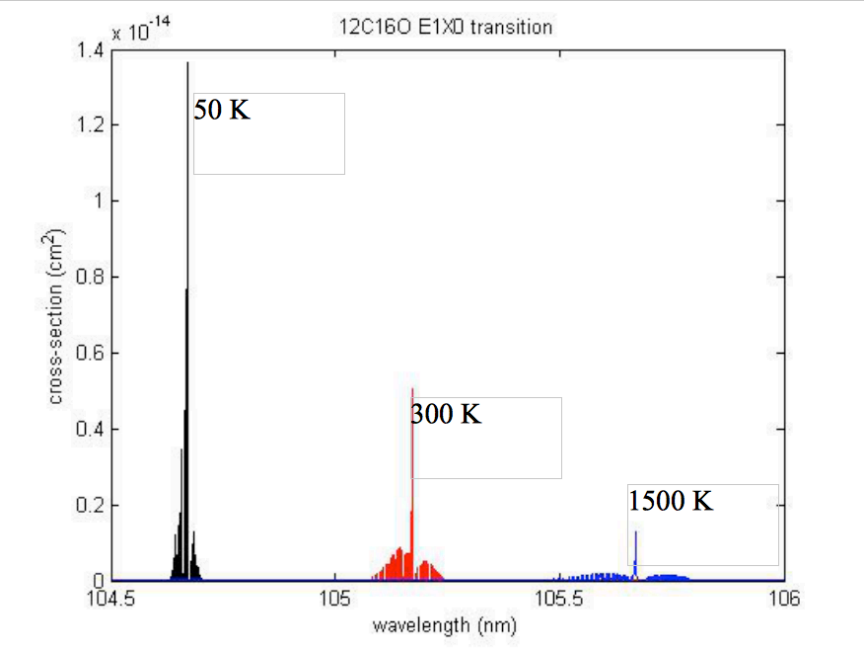

Figure 5.4: The synthetic $^{12}C^{16}O$ spectrum calculated at 50K (black), 300K (red), and 1500K (blue). The 50K and 1500K spectra have been shifted -/+0.5 nm respectively for clarity. The ratio of maxima is approximately 12:4:1.

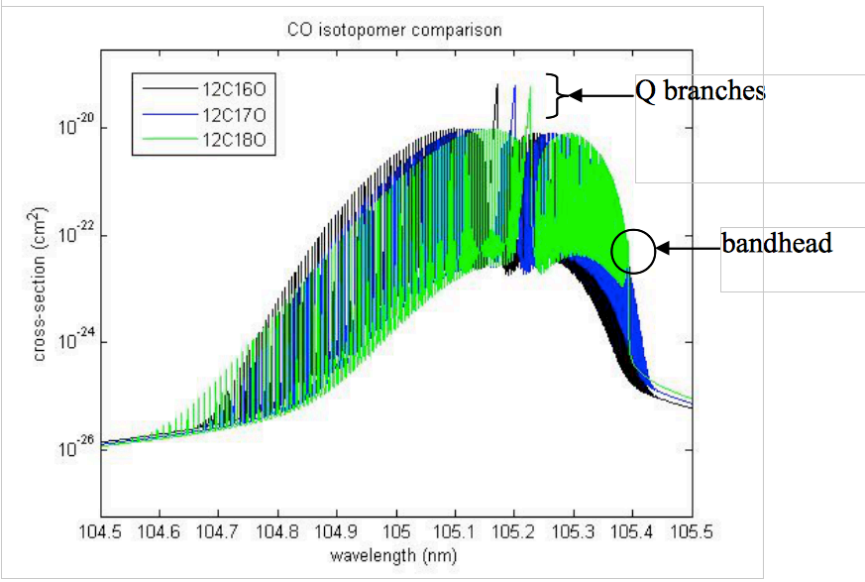

Figure 5.5: The spectra for the $X^1\Sigma_g^+(0)$ - $E^1\Pi(1)$ transition of $^{12}C^{16}O$, $^{12}C^{17}O$, and $^{12}C^{18}O$ at 1500 K

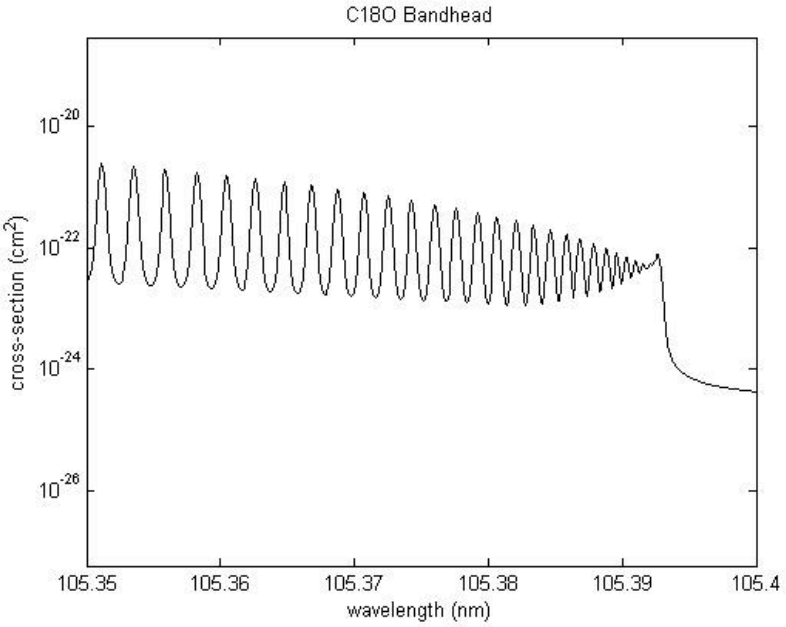

Figure 5.6: The bandhead in the $^{12}C^{18}O$ spectrum at 1500 K

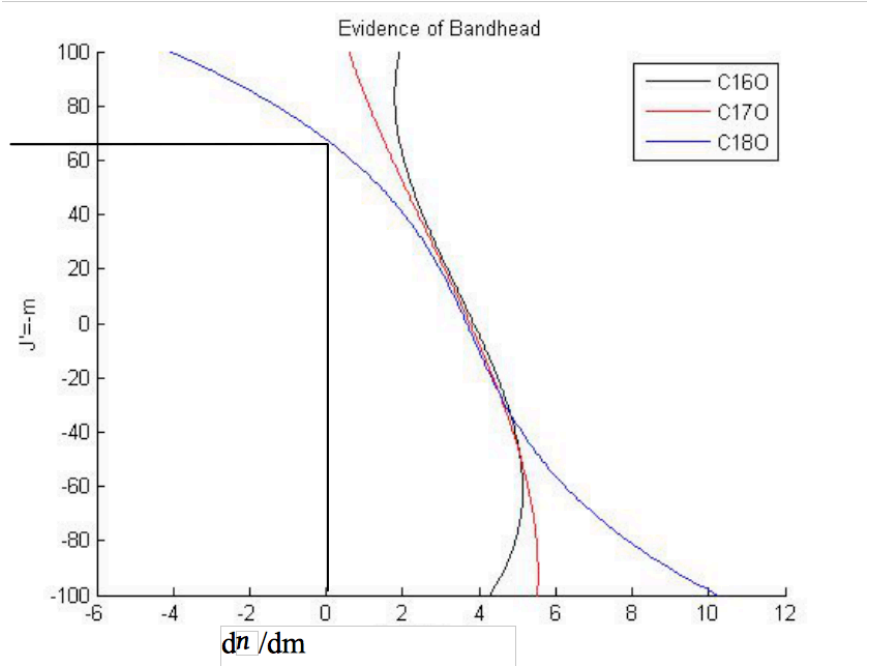

Figure 5.7: Evidence of a bandhead. This graph shows a bandhead between the 66th and 67th rotational state for $^{12}C^{18}O$.

and is presently designed for radiation incident along the Z-axis (see Fig. 5.1).

CO is produced and destroyed by many different reactions in the model. For loss of CO by photodissociation, L_i for each CO isotopologue is given by:

$$L_{C^xO} = \epsilon e^{-\tau_{abs}(z)} \Theta_{H_2}(z) \int_{band31} \sigma_{C^xO}(\lambda)\phi(\lambda)F_0(\lambda)e^{-\tau(\lambda,z)}d\lambda \tag{5.10}$$

where F_0 is the modern day solar flux over band 31, ϵ is a flux enhancement factor relative to the modern day sun (to account for the difference in brightness of the protonebular sun, $1< \epsilon <10^3$), f is the photodissociation quantum yield and is nearly unity for this band,[50;51] $\Theta_{H_2}(z)$ the shielding function for H_2,[67] and $\tau(\lambda, z) = \sum_i N_{C^xO}(z)\sigma_{C^xO}(\lambda)$ is the combined optical depth for the CO isotopologues, $N_{C^{16}O}$, $N_{C^{17}O}$, and $N_{C^{18}O}$ are the column densities of the respected isotopomers. Dust opacity, τ_{dust}, is identical for all isotopologues, and was parametrized in the same manner as is done for the interstellar medium. As mentioned earlier, we take the incoming radiation along the Z-direction in this model. As such, the column densities are obtained by integrating the Aikawa disk model (Eq. 5.2) for number densities for fixed R (along the z-direction). The shielding integrals describe the shielding effects of the various CO isotopologues upon each other, and are the sole source of non-mass dependent fractionation in our model. Using the shielding function for the H_2 number density does not take into account the effect of temperature on individual bands in H_2, but is a fit to the H_2 absorption line wings at low temperature; a more detailed consideration of H_2 temperature dependence will be found in the next section.

We assume all oxygen photodissociated from CO proceeds to H_2O by the following reactions:

$^XO + H_2 \xrightarrow{k_1} {}^XOH + H + H_2 \xrightarrow{k_2} {}^XOH_2 + H$

This is justified by calculating the k_1 and k_2 at 1500 K. Using experimental values and literature, closed-form temperature dependent approximations for k1[69] and k2[70] have previously been found. Using these empirical formulae evaluated at the temperature (1500 K) and number density (n(H2) 3.0x10^{18} cm^{-3}) of the mid-plane of the X-point we obtain k_1 ≈2.49 x 10^{-12} cm^3/s and k_2 ≈ 6.803 x 10^{-12} cm^3/s. These are bimolecular rate constants, and correspond to reaction time-scales of 1.3 x 10^{-7}s and 4.9 x 10^{-8} s respectively. This can be compared with another reaction which is very fast at the X-point:

$^XO + C^YO \xrightarrow{k_3} C^XO + {}^YO$

This reaction would scramble any isotope effect from shielding if the oxygen was not incorporated into water in reactions 1 and 2 very quickly. A closed-form temperature dependent model for k_3 has also been previously found.[71] At the X-pt., we find bimolecular k_3 1.00 x 10^{-11} cm^3/s and a timescale of 1.7 x 10^{-4} s. Thus, the incorporation of the isotope into water is 3-4 orders of magnitude faster than isotope scrambling by exchange with CO at the X-point, and our assumption of rapid incorporation of molecular oxygen into water appears justified.

Oxygen isotope composition for an unknown u was computed as:

$$\delta^X O_{CO_{initial}}(u) = 10^3((^X O)/^{16}O)_u/((^X O)/^{16}O)_{initial}) - 1) \tag{5.11}$$

for both O and CO in the nebula. Initial CO was assumed to have oxygen isotope ratios of $^{16}O/^{18}O = 500$ and $^{16}O/^{17}O = 2600$. The shift in isotopic composition for an unknown u from a CO initial reference to a standard mean ocean water (SMOW) reference is given by:

$$\begin{aligned}\delta^X O_{SMOW}(u) =& \delta^X O_{CO_{initial}}(u) \\ &+ \delta^X O_{SMOW}(CO_{initial}) + 10^{-3}\delta^X O_{initial}(u)\delta^X O_{SMOW}(CO_{initial})\end{aligned} \tag{5.12}$$

where x = 17 or 18, and $\delta^X O_{SMOW}(CO_{initial}) = -50\%o$. The oxygen isotope composition of total nebular H_2O is then given by:

$$\delta^X O_{SMOW}(H_2O_{tot}) = \frac{f_{H_2O_{cloud}}\delta^x O_{SMOW}(H_2O_{cloud}) + f_{H_2O_{ss}}(t)\delta^x O_{SMOW}(H_2O_{ss})}{f_{H_2O_{cloud}} + f_{H_2O_{ss}}(t)} \tag{5.13}$$

where the volume fraction of H_2O from the parent cloud is $f_{H_2O_{cloud}} = 2$ x 10^{-4} , the isotope composition of the H_2O in the cloud is $= -50$, $f_{H_2O_{ss}}(t)$ is the volume fraction of H_2O produced from CO photodissociation (H_2O_{ss}) , and x = 17 or 18.

One can see in Fig. 5.8, referred to as a 3-isotope plot, that at the X-pt. and subject to approximations elsewhere in this Chapter there is a self-shielding effect similar to that observed in CAIs (slope of 1) at 30 AU. Typically, materials found on Earth and in our solar system have a slope of 0.52, and this is the anamolous effect first discovered by Clayton.[46] Deviations above a slope of 1 in the first quadrant of a 3-isotope plot are the result of regions where ^{18}O is in isotopic excess compared to ^{17}O, when both are compared to levels found in SMOW. Deviations below indicate the reverse effect. We are constrained to the first quadrant (i.e. $\delta^{17}O_{SMOW}, \delta^{18}_{SMOW} > 0$) because the self-shielding process postulated by Clayton results in an abundance of these heavy isotopomers, which are then incorporated into solar nebular water.

5.4 Comparison with Navon and Wasserburg

Navon and Wasserburg[61] carried out a similar calculation for the hypothesis of O_2 self-shielding at lower temperatures as an explanation of anomalous isotope ratios in CAIs. Their analysis differed from ours in that they approximated each rovibrational line as a product of step-up and step-down functions added to a pseudocontinuum.

They concluded that O_2 self-shielding was not a valid explanation because the $^{16}O^{17}O$ and

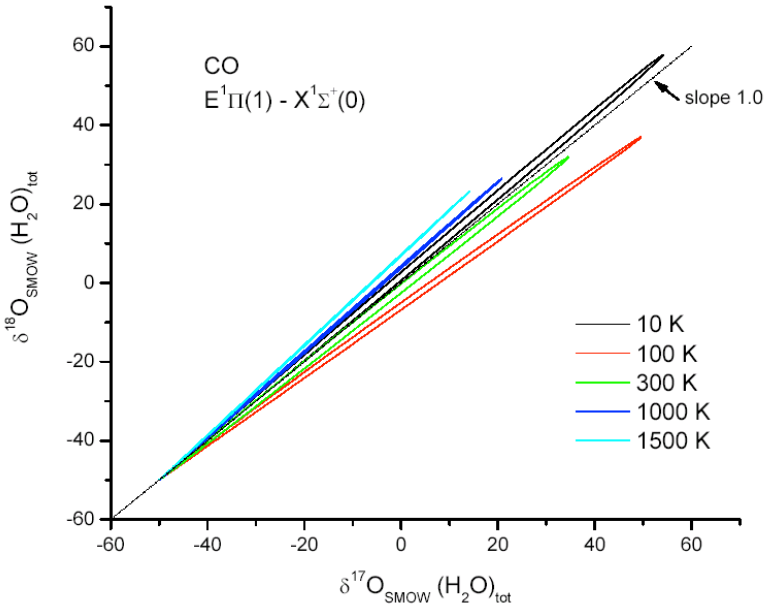

Figure 5.8: 3-isotope plot at 30 AU with temperature dependent CO cross sections. H_2 absorption by shielding function.[7]

$^{16}O^{18}O$ spectra were enveloped by the $^{16}O^{16}O$ spectrum, even at the low temperatures in their hypothesis (T = 300 K). This result was apparent despite their lineshape approximation because the natural linewidth of O2 is much greater than CO, about a factor of 100 higher.[61]

For comparison with our spectroscopic results, consider the following. We have carried out an identical analysis for the ^{12}CO isotopomers $^{12}C^{17}O$ and $^{12}C^{18}O$, modifying the linewidth by the appropriate factor of 100 to see if our results agree with those of Navon and Wasserburg.[61] The resulting spectra (overlaid in Fig. 5.9) show that the $^{12}C^{17}O$ and $^{12}C^{18}O$ are indeed completely enveloped, resulting in no observed self-shielding. As a result, we have confidence both in the absence of O_2 self-shielding and of CO self- shielding at the X-point in the absence of other protonebular considerations (see next section for discussion).

5.5 Absorption by H_2

Differential mutual shielding by H_2 is accounted for by modifying Eq. 5.10 such that:

$$L_{C^xO} = \epsilon e^{-\tau_{dust}(z)} \int_{band31} \sigma_{C^xO}(\lambda)\phi(\lambda)F_0(\lambda)e^{-\tau(\lambda,z)}d\lambda \tag{5.14}$$

where now $\tau(\lambda, z) = \sum N_{C^iO}(z)\sigma_{C^iO}(\lambda) + N_{H_2}(z)\sigma_{H2}(\lambda)$, σ_{H_2} is the cross-section of molecular

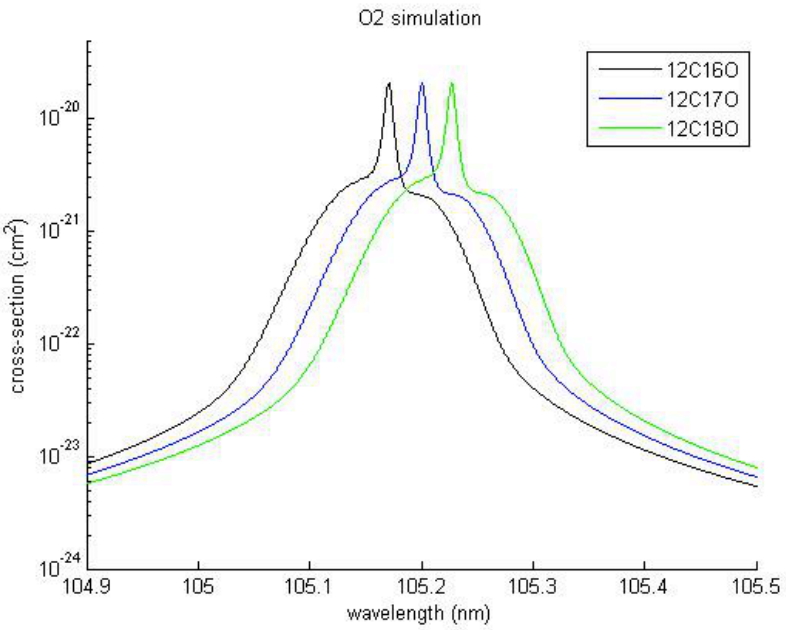

Figure 5.9: The three isotopomers of $^{12}C^{x}O$ with a fictitiously high natural linewidth are compared.

Hydrogen, obtained from an earlier synthetic spectrum,[7] N_{H_2} is the column density of H_2, and the rest of these parameters are the same as in Eq. 5.10.

The Q-branch of band #31 in $^{12}C^{17}O$ is situated precisely in a broad H_2 transmission feature, see Fig. 5.10 (a)-(c). This coincidence negates any predicted CO isotope effect due to band #31 (see Fig. 5.11). This band dominates CO dissociation, and, as such, we do not expect the self-shielding of our pseudo-Clayton model to be a plausible mechanism at the temperatures found in the X-point, due to H_2 self-shielding.

5.6 Conclusions

We find that, for absorption band #31 of CO, our simple model for self-shielding is insufficient to obtain the mass-independent oxygen isotope effect conclusively. This is caused by a coincidence of the $C^{17}O$ Q-branch with a transmission feature of H_2. This effect was evaluated for a pseudo-Clayton model where incident light comes from the outside the disk but with the intensity of the proto-sun. Note that this conclusion also suggests that, in a colder environment such as that further away from the X-point, the hydrogen cross-section will be considerably less and so this self-shielding effect will not be masked by this coincidence.

More work is needed to determine the effects of electronic perturbation, additional predissociative states, and additional chemical processes present after photodissociation at the X-point in this calculation. At such high temperatures, in the case that self-shielding does occur, additional

(a)

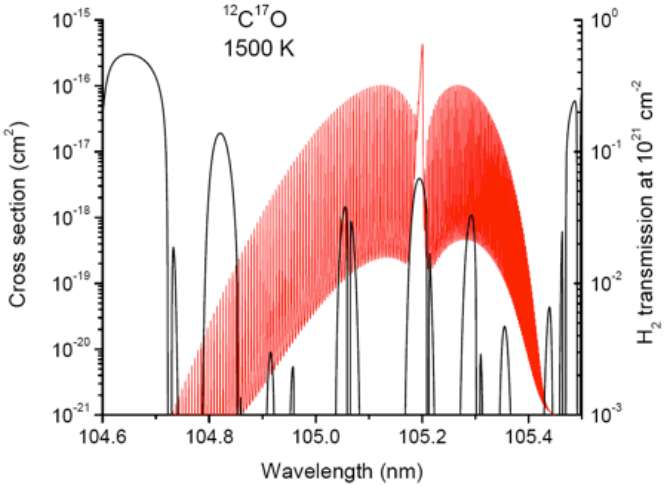

(b)

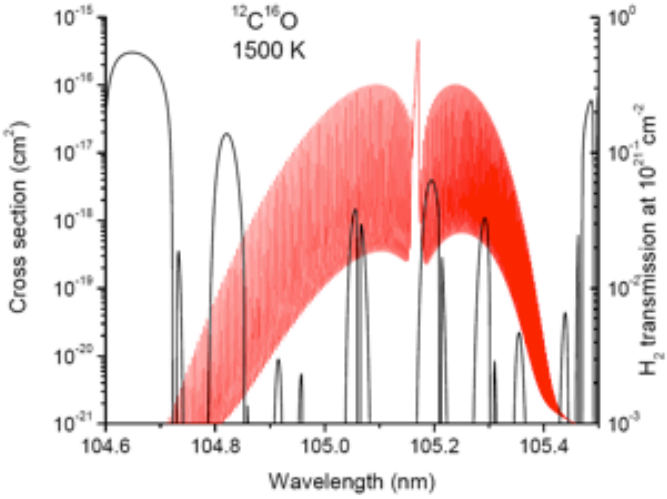

(c)

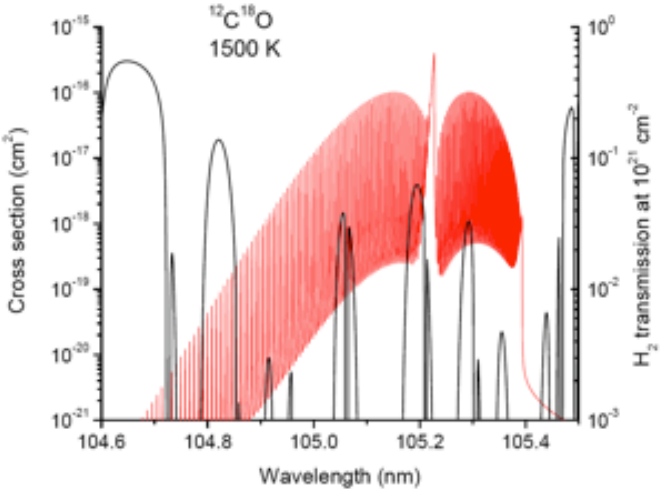

Figure 5.10: (a) $^{12}C^{17}O$, (b) $^{12}C^{16}O$, and (c) $^{12}C^{18}O$ cross section (red) with overlay of H_2 transmission (black). Q-branch of $C^{17}O$ coincides with H_2 transmission feature causing the vertical 3-isotope trajectory at high temperatures.

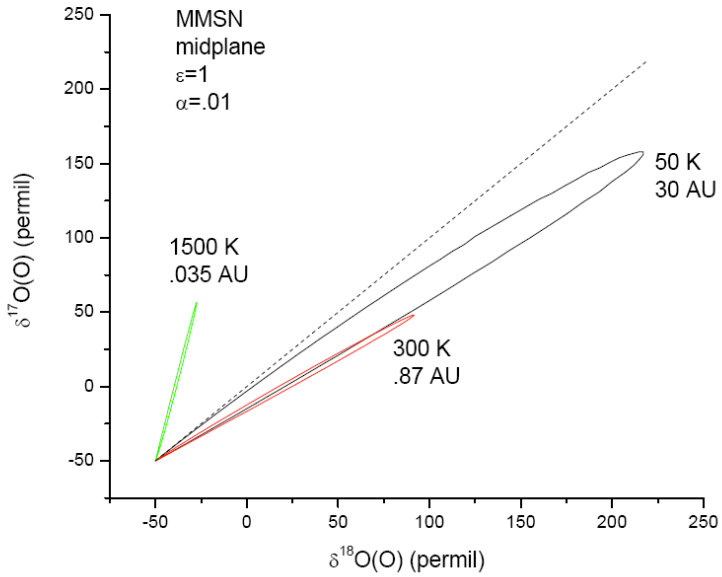

Figure 5.11: 3-isotope plot with H_2 absorption cross sections at 0.035 AU, 0.87 AU, and 30 AU at the mid-plane (Z=0).

reactions take place that could potentially skew the effect further.

5.7 Chapter Appendix: Voigt Profile Approximation

The Voigt profile is a convolution of a Gaussian and Lorentzian lineshape, and has the general formula:[65]

$$f_v(v - v_0) = \int_{-\infty}^{\infty} f_L(v' - v_0) f_D(v - v')dv' \tag{5.15}$$

where $f_L(v' - v_0)$ and $f_D(v - v')$ are the familiar Lorentzian and Doppler lineshapes respectively and v_0 is the line position. Including the specific forms these more well known lineshapes we arrive at the following form of the Voigt profile:

$$f_v(v - v_0) = \frac{\alpha_L}{\pi^{3/2}\alpha_D} \int_{-\infty}^{\infty} \frac{1}{(v' - v_0)^2 + \alpha_L^2} exp(-\frac{(v - v')^2}{\alpha_D^2})dv' \tag{5.16}$$

where α_L , and α_D are the Lorentzian and Doppler widths. The Lorentzian width is assumed to be the natural linewidth 0.034 cm^{-1}. The Doppler width is given by $\alpha_D = v_0/c(2RT)^{1/2}$ where v_0 is the central frequency of the rovibrationalline , c the speed of light, R the individual gas constant,

and T the temperature. We make the approximation of the Voigt profile as :

$$f_v(v-v_0) = (\frac{ln2}{\pi})^{1/2}\frac{1}{\alpha_v}(1-\xi)exp(-\eta^2 ln2) + \frac{\xi}{\pi\alpha_v(1+\eta^2)} \tag{5.17}$$

$$- \frac{\xi(1-\xi)}{\pi\alpha_v}(\frac{1.5}{ln2} + 1 + \xi)(0.66exp(-0.4\eta^2) - \frac{1}{40-5.5\eta^2+\eta^4}) \tag{5.18}$$

where $\xi = \alpha_L/\alpha_v$, $\eta = (v-v_0)/\alpha_v$, and the Voigt half-width, α_v, is given by

$$\alpha_v = 0.5[\alpha_L + (\alpha_L^2 + 4\alpha_D^2 ln2)^{1/2}] + 0.05\alpha(1 - \frac{2\alpha_L}{\alpha_L + (\alpha_L^2 + 4\alpha_D^2 ln2)^{1/2}} \tag{5.19}$$

It is this closed form of the Voigt profile from the literature[65] used in the present calculations.